Stationary shear flow around fixed and free bodies at finite Reynolds number

By DUANE R. MIKULENCAK[1]† AND JEFFREY F. MORRIS[2]‡

[1]School of Chemical Engineering, Georgia Institute of Technology, Atlanta, GA 30332, USA

[2]Halliburton, 3000 N. Sam Houston Parkway, Houston, TX 77032, USA

Numerical solutions of stationary flow resulting from immersion of a single body in simple shear flow are reported for a range of Reynolds numbers. Flows are computed using finite-element methods. Comparisons to results of asymptotic low-Reynolds-number theory, experimental study, and other numerical techniques are provided. Results are presented primarily for isotropic bodies, i.e. the circular cylinder and sphere, for both of which the two conditions of a torque-free (freely-rotating) and fixed body are investigated. Conditions studied for the sphere are $0 < Re \leqslant 100$, and for the circular cylinder $0 < Re \leqslant 500$, with the shear-flow Reynolds number defined as $Re = \dot{\gamma}a^2/\nu$; $\dot{\gamma}$ is the shear rate of the Cartesian simple shear flow $\boldsymbol{u} = (\dot{\gamma}y, 0, 0)$, a is the cylinder or sphere radius, and ν is the kinematic viscosity of the fluid. In the torque-free case, the rotation rate of the body decreases with increasing Re. Qualitative dependence, seen in the $Re = 0$ fluid flow field, upon whether the body is fixed against rotation or torque-free vanishes as Re increases and the fluid flow is more similar to that around the $Re = 0$ fixed body: the influence of rotation of the body and the associated closed streamlines are confined to a narrow layer about the body for $Re > O(1)$. Separation of the boundary layer is observed in the case of a fixed cylinder at $Re \approx 85$, and for a fixed sphere at $Re \approx 100$; similar separation phenomena are observed for a freely rotating cylinder. The surface stress and its symmetric first moment (the stresslet) are presented, with the latter providing information on the particle contribution to the mixture rheology at finite Re. Stationary flow results are also presented for elliptical cylinders and oblate spheroids, with observation of zero-torque inclinations relative to the flow direction which depend upon the aspect ratio, confirming and extending prior findings.

1. Introduction

This work describes simple shear flow around isolated bodies at finite Reynolds number. We consider primarily the geometries of circular cylinder and sphere, but will also present results for inertial shear flow about elliptical cylinders and oblate spheroids. Analytical Stokes-flow solutions for shear flow around the sphere and circular cylinder are well known, but the role of inertia upon the fluid motion is not thoroughly understood. This lack of detailed understanding of particle-scale shear flows hinders both progress in describing hydrodynamic interactions in inertial

---

† Present address: Shell Exploration and Production Company, 701 Poydras Street, New Orleans, LA 70139, USA.
‡ Author to whom correspondence should be addressed: jeff.morris2@halliburton.com

suspension flows and development of the averaged-equation description of such flows (Koch & Hill 2001; Sundaresan *et al.* 2003). The limited understanding of inertial effects at the single-body level in shear flows is surprising given the abundant study of bodies in a uniform stream, as well as recent many-particle shear-flow simulations at finite Reynolds number (e.g. Huang & Joseph 2000). However, the literature provides little description of inertial shear flow alone, i.e. without a uniform component, about isolated bodies.

The primary goal of this work is to improve upon this situation by establishing, through solutions obtained numerically, a detailed description of the stationary flows resulting from a single cylinder or sphere in a simple shear flow over a wide range of Reynolds number. The Reynolds number for the simple shear flow is defined on the scale of the body as $Re = \dot{\gamma}a^2/\nu$, where $\dot{\gamma}$ is the shear rate, ν is the fluid kinematic viscosity, and a is the radius of the sphere or cylinder. When describing results from other work, we convert to this definition of the Reynolds number if necessary.

Particle interactions with flowing fluid are basic to the study of diverse topics. For a body and fluid in relative translational motion at a speed U, the inertia is defined by the translational Reynolds number, $Re_U = UL/\nu$ with L the characteristic size of the body. The resulting flow may represent situations ranging from sedimentation of silt at essentially vanishing inertia to projectile motion where $Re_U \gg 1$. Results from prior work in this area for simple geometries are abundant. Among these are results which have long been textbook material, such as the drag force, known over a wide range of Re_U and typically expressed in dimensionless form as the drag coefficient. This wealth of knowledge is not mirrored when consideration is broadened to linear flows.

We consider a particle in the undisturbed simple shear flow given by $\boldsymbol{u}^\infty = (u_x, u_y, u_z) = (\dot{\gamma}y, 0, 0)$. Recalling that simple shear flow is composed in a kinematic sense of equal parts rotational and extensional flow, pure extension is a more basic flow, but simple shear has certain advantages. From a numerical perspective, steady simple shear is convenient because it is an exact solution of the Navier–Stokes equations for any value of the Reynolds number. Simple shear flow may also be experimentally approximated more simply, and critically over much larger experimental test volumes, than extensional flow (Higdon 1993).

Experimental study of flow around cylinders symmetrically placed in simple shear, such that they experience zero net force, has been performed by Poe & Acrivos (1975), who found good agreement with the numerical results of Kossack & Acrivos (1974) for $Re < 6$ with loss of steadiness for larger Re. This loss of steadiness appears to have been due to experimental difficulties, as more recent study of the shear flow around a circular cylinder by Zettner & Yoda (2001a) for $0 < Re < 20$ found steadiness at all conditions. These studies found that the rotation speed decreased with Re and demonstrated some asymmetry in flow patterns, all for unseparated flow. Little analogous experimental work has examined the role of inertia on the local flow around force-free spheres in simple shear although some results have been provided by Poe & Acrivos. Note that the influence of force-free spheres and cylinders upon fluid mechanical features at much larger scale, including streamwise vortex generation near turbulence onset, has been demonstrated (Bottin, Dauchot & Daviaud 1997; Bottin *et al.* 1998).

As evidenced by the scarcity of studies devoted to the topic, experimental study of shear flow about suspended particles presents a number of difficulties, especially if interest is in the force-free case. Numerical studies are arguably more convenient and certainly provide results of greater detail. We study the case of a particle symmetrically

placed in the shear flow $\boldsymbol{u}^{\infty}$ described above such that it is free of a net hydrodynamic force, and examine both the freely-rotating (zero net torque) and fixed conditions. One motivation is that, in the freely rotating case, the flow and particle-induced stress have direct relevance to suspension mechanics at finite-particle-scale inertia. The resulting flow corresponds physically to the flow observed from the frame of reference of a neutrally buoyant particle released in an infinite simple shear flow after allowing the body to take on the force- and torque-free motion.

Work addressing inertial stresses in a dilute suspension by Lin, Peery & Schowalter (1970) was initiated at about the time that Batchelor (1970) described the stress system in a suspension of force-free particles, but suspension stress at finite Re remains very poorly understood relative to the $Re = 0$ case. Most analysis at finite inertia has been limited to $Re \ll 1$, where matched asymptotic expansions have been used to analyse weakly inertial simple shear flow about a circular cylinder by Robertson & Acrivos (1970) and about a sphere at finite Re by Lin *et al.* The same methodology, augmented by the Lorentz reciprocal theorem (Kim & Karrila 1991), has been used to examine the role of weak inertia in a general linear flow around an immersed sphere by Stone, Brady & Lovalenti (2001). Loss of fore–aft symmetry of the flow about an isotropic body leads to predictions of finite normal stress differences (absent for a single sphere at $Re = 0$ owing to symmetries of both body and flow), in addition to inertial effects upon the dilute suspension viscosity. Dilute suspension viscosity in axisymmetric extension about a single sphere for Re up to $O(1000)$ was studied by Ryskin (1980) using a vorticity–streamfunction formulation.

Numerical studies have provided some insight into inertial effects at higher Re. The flow about a symmetrically placed cylinder in simple shear was approximated using a finite-difference method by Kossack & Acrivos (1974) for $0 < Re < 70$; we note that our work suggests certain streamline plots in this reference (e.g. their figure 7*a* at $Re = 10$) are inverted in the shear gradient direction. The analogous problem for a sphere in simple shear has been studied by Nirschl, Dwyer & Denk (1995) for a wall-bounded geometry at $0.025 < Re < 25$ using a finite-volume scheme. The influence of inertial flow upon the rheology of a dilute suspension of disks was performed by Patankar & Hu (2002); from finite-element-based numerical solutions of simple shear around a circular cylinder, Patankar & Hu extracted the first normal stress difference (the second normal stress difference is undefined in this case) up to $Re = 5$.

It is worth noting that there exist a number of finite-Reynolds-number numerical studies examining linear flow combined with a uniform translation past particles. Examples include those of Dandy & Dwyer (1990) who studied uniform motion plus simple shear, and of Bagchi & Balachandar (2002, 2003) who have provided a thorough examination for a sphere immersed in combined uniform flow and extensional flow as a function of Reynolds number. However, neither of these, nor to our knowledge any other, studies addressing uniform-plus-linear flow considered the problem of a force-free particle which is our focus.

In this work, we present velocity and pressure fields around suspended bodies computed using finite-element methods. We also provide results demonstrating the evolution with Re of the contribution to the bulk stress due to the surface stresses on the particle. In the following section, the problems are defined and the methods used for their numerical solution are presented; the validation of the method includes results for non-isotropic particles in shear flow. In §3, we first give analytical results in the Stokes- and potential-flow limits, followed by computed results for shear flows about spheres and cylinders, dividing these according to whether the inertia is weak to moderate ($0 < Re \leqslant 10$) or strong ($Re > 10$). In §4, results are given on the rotation

rate and the stresslet (symmetric first moment of the surface stress) of particles in simple shear flow over a range of *Re*.

2. Governing equations and numerical technique

2.1. *Problem formulation*

We present here a general problem formulation used for all flow computations in this work. We consider a neutrally buoyant rigid particle of size a immersed in fluid that is undergoing simple shear flow, $u^\infty = (\dot{\gamma} y, 0, 0)$, at the outer boundary, which in the ideal case would be taken infinitely far from the particle. For spheres and circular cylinders, a is the radius, while for spheroids or elliptical cylinders, a is the half-length of the major axis. We take the origin to be the centre of the particle. The 1 or flow direction is denoted by x, the 2 or velocity gradient direction by y, and the 3 or vorticity direction by z. The flow is governed by the steady Navier–Stokes equations for fluid of kinematic viscosity $\nu = \mu/\rho$, with μ the dynamic viscosity and ρ the density,

$$\nabla \cdot u = 0, \quad Re\,(u \cdot \nabla)\,u = -\nabla p + \Delta u, \tag{1}$$

shown in dimensionless form. Here and below, the position vector x is scaled by a, the fluid velocity u by $\dot{\gamma} a$, and the pressure p by the characteristic viscous stress $\mu \dot{\gamma}$. The particle shear-flow Reynolds number is defined as $Re = \dot{\gamma} a^2/\nu = \rho \dot{\gamma} a^2/\mu$.

On the surface of the particle, the fluid velocity matches that of the body, and thus is required to be either zero for the fixed body, or to be in rigid body rotation at rate $\boldsymbol{\Omega}$ such that the particle experiences no hydrodynamic torque. Owing to the symmetry of the shear flow and the particle geometry, the rotation rate is anticipated to be of the form $\boldsymbol{\Omega} = \Omega e_z$. Finally, far from the particle, the velocity should return to the imposed simple shear flow. The boundary conditions applied to (1) are thus

$$u = \boldsymbol{\Omega} \times x, \tag{2}$$

on the particle surface and

$$u = \dot{\gamma} y e_x, \tag{3}$$

on the outer boundary. In computing numerical solutions to (1), we truncate our fluid domain either by a bounding rectangular box or a bounding outer surface of the same geometry as the immersed particle. This outer boundary for the particle-shaped domain is characterized by the geometric parameter R^∞. For an isotropic domain, R^∞ is the outer radius, whereas it is the minor axis half-length for an anisotropic (elliptical or ellipsoidal) domain. The manner of imposing the condition (3) will depend on the mesh design used to solve the flow problem in its discretized form, as described in §2.3.

For freely suspended particles in shear flow, the boundary condition (2) is not straightforward since the torque-free rotation rate is unknown for arbitrary *Re*, and thus

$$T(\Omega) = \int_{\Gamma_p} [x \times (\sigma(\Omega) \cdot n)] \cdot e_z \, \mathrm{d}x = 0, \tag{4}$$

must be solved for the appropriate Ω. Here, n is the normal vector pointing out of the particle and σ, the fluid stress, is a function of Ω through the boundary condition (2) used in determining u. Applying Newton's method to (4) results in the following linearization, which we set to zero (hence the final equality) based on the smallness

of the torque for satisfactory solutions,

$$T(\Omega^{k+1}) \approx T(\Omega^k) + \frac{\partial T}{\partial \Omega}(\Omega^k)(\Omega^{k+1} - \Omega^k) = 0, \tag{5}$$

where k is an iteration index. Using $\partial T/\partial \Omega(\Omega^k) \approx (T(\Omega^k + \Delta\Omega) - T(\Omega^k))/\Delta\Omega$ in (5) yields

$$\Omega^{k+1} = \Omega^k - \frac{T(\Omega^k)}{(\partial T/\partial \Omega)(\Omega^k)}. \tag{6}$$

Given Ω^0, we seek to determine $\boldsymbol{u}$ numerically by solving (1) and (2) with $\Omega = \Omega_0$. Compute $T(\Omega^0)$ from (4) and for $k = 0, 1, 2, \ldots$ perform the following steps: (i) solve (1) and (2) with $\Omega = \Omega_k + \Delta\Omega$; (ii) compute $T(\Omega_k + \Delta\Omega)$; (iii) compute $(\partial T/\partial \Omega)(\Omega^k)$ from the difference formula; (iv) determine Ω^{k+1} from (6); (v) solve (1) and (2) with $\Omega = \Omega_{k+1}$ and compute $T(\Omega_{k+1})$. Taking $\Delta\Omega = 0.001$ works well in practice. Iteration is continued until $T < 0.0001$, which typically occurs in only one or two iterations for a reasonable initial guess (e.g. a previously computed Ω from a nearby Re).

2.2. *Finite-element solution method*

We have used a finite-element approach, with two different flow solvers, to construct approximate solutions to the Navier–Stokes equations. The direct solver, detailed in §A.1, uses Newton's method for the nonlinearity coupled with MATLAB's linear systems sparse solver and is our preferred method for two-dimensional problems. For three-dimensional problems with their larger computational and storage requirements, §A.2 presents an iterative solver that employs a conjugate gradient linear solver with a nonlinear least-squares conjugate gradient method to resolve the nonlinearity. This flow solver is attractive because it requires relatively small memory.

We begin with a generic version of (1) in dimensional form

$$\begin{rcases} \nabla \cdot \boldsymbol{u} = 0, \\ \rho(\boldsymbol{u} \cdot \nabla)\boldsymbol{u} - \mu\Delta\boldsymbol{u} + \nabla p = \boldsymbol{f} \text{ in } V_f, \\ \boldsymbol{u} = \boldsymbol{g} \text{ on } \Gamma, \end{rcases} \tag{7}$$

where $V_f \subset \boldsymbol{R}^n$ with $n = 2$ or 3, $\Gamma \subset \boldsymbol{R}^{n-1}$ denotes the boundary, $\boldsymbol{u} : V_f \to \boldsymbol{R}^n$ denotes the fluid velocity, $p : V_f \to \boldsymbol{R}^n$ is the fluid pressure, and $\boldsymbol{f}$ is a forcing term that is either a physical body force or comes from a nonlinear iteration scheme. We solve for the full velocity field $\boldsymbol{u}$ rather than the disturbance velocity in order to take advantage of existing iterative methods developed for the structure of the basic Navier–Stokes equations. Integrating (7) against smooth test functions, $\{\boldsymbol{v} : V_f \to \boldsymbol{R}^n, \boldsymbol{v} = 0 \text{ on } \Gamma\}$ and $\{q : V_f \to \boldsymbol{R}\}$ leads to the weak or generalized form:

$$\begin{rcases} \displaystyle\int_{V_f} (\nabla \cdot \boldsymbol{u})q \, \mathrm{d}\boldsymbol{x} = 0, \\ \displaystyle\int_{V_f} \rho[(\boldsymbol{u} \cdot \nabla)\boldsymbol{u}] \cdot \boldsymbol{v} \, \mathrm{d}\boldsymbol{x} + \int_{V_f} \mu\nabla\boldsymbol{u} : \nabla\boldsymbol{v} \, \mathrm{d}\boldsymbol{x} - \int_{V_f} p(\nabla \cdot \boldsymbol{v}) \, \mathrm{d}\boldsymbol{x} = \int_{V_f} \boldsymbol{f} \cdot \boldsymbol{v} \, \mathrm{d}\boldsymbol{x}. \end{rcases} \tag{8}$$

A solution requires that $\boldsymbol{u} \in H^1(V_f) = \{\boldsymbol{y} : |\boldsymbol{y}|, |\nabla\boldsymbol{y}| \in L^2(V_f)\}$, $\boldsymbol{v} \in H_0^1(V_f) = \{\boldsymbol{y} : \boldsymbol{y} \in H^1(V_f), \ \boldsymbol{y} = 0 \text{ on } \Gamma\}$, and $p, q \in L^2(V_f)$. Solutions $(\boldsymbol{u}, p)$ and test functions $(\boldsymbol{v}, q)$ must have at least these minimal regularity properties: velocity trial and test functions and their derivatives must be square integrable, and pressure trial and test functions must be square integrable.

We now define the finite-element solution of the problem as

$$
\left.
\begin{aligned}
\int_{V_f} (\nabla \cdot \boldsymbol{u}_h) q_h \, \mathrm{d}\boldsymbol{x} &= 0, \\
\int_{V_f} \rho[(\boldsymbol{u}_h \cdot \nabla)\boldsymbol{u}_h] \cdot \boldsymbol{v}_h \, \mathrm{d}\boldsymbol{x} + \int_{V_f} \mu \nabla \boldsymbol{u}_h : \nabla \boldsymbol{v}_h \, \mathrm{d}\boldsymbol{x} - \int_{V_f} p_h(\nabla \cdot \boldsymbol{v}_h) \, \mathrm{d}\boldsymbol{x} &= \int_{V_f} \boldsymbol{f} \cdot \boldsymbol{v}_h \, \mathrm{d}\boldsymbol{x}, \\
\boldsymbol{u}_h &= \boldsymbol{g} \text{ on } \Gamma,
\end{aligned}
\right\} \quad (9)
$$

where $\boldsymbol{u}_h \in \hat{V}_h \subset H^1(V_f)$, $\boldsymbol{v}_h \in V_h \subset H_0^1(V_f)$ and p_h, $q_h \in Q_h \subset L^2(V_f)$ with h indicating a finite dimensional space. The space in which the unknown solution, $\boldsymbol{u}$ or p, is approximated is known as the trial space, while the space of weights, $\boldsymbol{v}$ or q, is known as the test space. For this Dirichlet problem, the pressure level must also be specified, accomplished here by setting the pressure at one point on the outer boundary to zero.

We discretize using the MINI element (Arnold, Brezzi & Fortin 1984), defined by approximating the pressure trial and test spaces by piecewise linear and continuous functions on a triangular or tetrahedral mesh. These functions are taken to be the standard $P1$ interpolating functions (Thommaset 1981). A basis for this space is the set of linear, continuous functions $\{\psi_i\}$ with $\psi_i = 1$ at vertex i and $\psi_i = 0$ at all other vertices in the mesh. Hence, the dimension of the pressure space is equal to the total number of vertices in a mesh, N_N, less one for specifying the pressure level ($\approx N_N$ for further discussion). Given this basis, the pressure can be expanded as $p_h = \sum_{j=1}^{N_N} P_j \psi_j$ so that P_j is the value of the pressure at vertex j.

The velocity trial and test spaces are constructed from the same piecewise linear and continuous functions defined on the same mesh. They are augmented by additional functions, known as bubble functions, which are piecewise cubic polynomials for triangular meshes and piecewise quartic polynomials for tetrahedral meshes. One particular basis for the bubble functions is defined such that $\phi_i = 1$ at the centroid of simplex i and $\phi_i = 0$ along its boundary as well as the rest of the domain. The total dimension of the velocity test space is then $n(N_N + N_L)$, where N_L is the number of simplices in a mesh. (To be precise, since $\boldsymbol{u}$ is prescribed on Γ, the dimension is actually $n(N_N + N_L - N_D)$, where $N_D \ll N_N + N_L$ is the number of vertices that lie on Γ.) The velocity can then be written as $\boldsymbol{u}_h = \sum_{j=1}^{N_N+N_L} \boldsymbol{U}_j \phi_j$. For $j = 1, \ldots, N_N$, ϕ_j is ψ_j, and $\boldsymbol{U}_j$ is the velocity at vertex j. The remaining $\boldsymbol{U}_j$ are regarded as stability parameters, paired with the bubble functions, and have no direct correspondence to the value of the velocity at the simplex centroid.

Recall that direct methods are used in this study for solving the flow in two dimensions, while an iterative method is employed for three-dimensional problems. Detailed descriptions of these methods are found in the Appendix.

2.3. *Finite-element mesh design*

We use triangular meshes for problems in the plane and tetrahedral meshes for three-dimensional problems. For shear flow past a sphere with $Re < 10$, we use structured tetrahedral meshes based on the underlying structure of the spherical annulus. The mesh is made by starting with the octant $x \geqslant 0$, $y \geqslant 0$, $z \geqslant 0$. Spherical coordinates are used to describe the spherical annulus and the azimuthal angle is divided by 12 vertices into 11 segments of $\pi/24$. Likewise, the polar angle is divided by 12 vertices into 11 segments of $\pi/24$. The radial direction is discretized to allot more points near
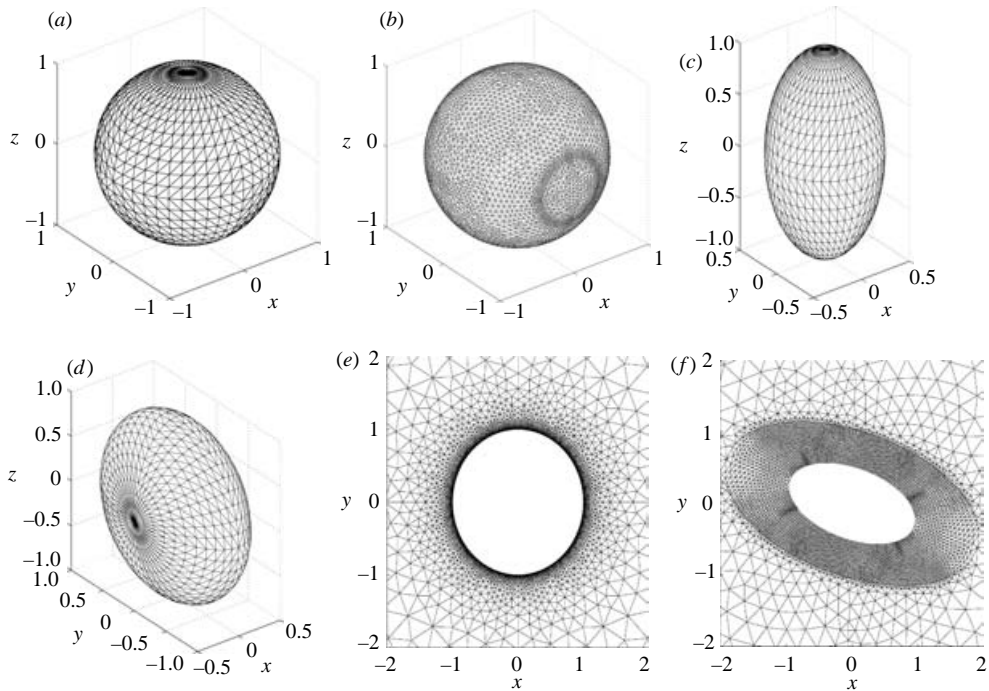
FIGURE 1. The mesh on the particle surface for flow computation for shear flow (*a*) past a sphere up to $Re = 10$, (*b*) a sphere at $Re > 10$, (*c*) a prolate spheroid, and (*d*) an oblate spheroid. A portion of the mesh used for flow field computation for shear flow past (*e*) a cylinder and (*f*) an elliptical cylinder.

the surface. This is accomplished by taking

$$\left.\begin{aligned} r_j &= \exp\left[\frac{j\log 2}{9}\right], \quad j = 0, 1, \ldots, 9; \\ r_j &= \exp\left[\log 2 + (j-9)\frac{\log 10 - \log 2}{5}\right], \quad j = 10, 11, \ldots, 14; \\ r_j &= \exp\left[\log 10 + (j-14)\frac{\log 50 - \log 10}{5}\right], \quad j = 15, 16, \ldots, 19; \\ r_j &= \exp\left[\log 50 + (j-19)\frac{\log 100 - \log 50}{2}\right], \quad j = 20, 21. \end{aligned}\right\} \quad (10)$$

Each (r, ϕ, θ) interval is then divided into six tetrahedra. Finally, the mesh is completed over the full space by reflections into the other octants. This gives 926 vertices on the sphere surface, or any constant radius surface, as shown in figure 1(*a*).

The formulae for the radial discretization define a family of meshes indexed by j with different sized outer boundaries. For example, taking $j = 0, 1, \ldots, 14$ gives a mesh described by $R^\infty = 10$ while taking $j = 0, 1, \ldots, 21$ gives $R^\infty = 100$. Computations from meshes with differing R^∞ thus share identical vertices for the intersection of the two vertex sets.

For oblate and prolate spheroids, the mesh was generated in the same manner as above, but using prolate or oblate spheroidal coordinates (Moon & Spencer 1971) rather than spherical coordinates. Consequently, the spheroids also have 926 vertices

on their surfaces and any conforming surface. The surface meshes are shown in figure 1(*c, d*). The oblate meshes are also rotated about the azimuthal angle. The oblate meshes only have mesh symmetry with respect to the $z = 0$ plane.

For high *Re* computations in the box domain, we use an unstructured mesh. This facilitates using a very high concentration of vertices near the particle surface to resolve sharp gradients without having the total number of vertices become prohibitively large. The mesh was computed using the FEMLAB mesh generator. The parameters used in the mesh generation were designed to concentrate more mesh points near the particle surface. A mesh discretization for the sphere surface is shown in figure 1(*b*). The mesh was generated in this manner for the quadrant $x \geqslant 0$, $y \geqslant 0$, $z \geqslant 0$ and then reflected into the full space to enforce the symmetries in the flow problems. Figure 1(*b*) shows the 4782 vertices that lie on the sphere surface of the mesh.

For two-dimensional computations, we use unstructured grids. For shear flow past cylinders, the cylinder surface is discretized with 628 vertices and is shown in figure 1(*e*). The cylinder mesh has symmetry with respect to both *x* and *y* axes. The mesh used for flow past an ellipse is also shown in figure 1(*f*) and has 160 vertices on the ellipse surface.

While the boundary condition of no-slip at the body surface is independent of the domain, different outer boundary conditions are applied depending upon whether the annular or box domain is employed. For small to moderate inertia, $Re < 10$, we use a spherical annulus of outer radius R^∞ as domain. In this case, the outer boundary condition is a direct return to simple shear on the outer boundary, $\boldsymbol{u} = \boldsymbol{u}^\infty$ at $r = R^\infty$, with $\boldsymbol{u}^\infty = \dot{\gamma} y \boldsymbol{e}_x$. For the spheroidal domains used with anisotropic bodies, the same form of outer boundary condition was used, although larger *Re* were considered here. For the box domain employed at large *Re*, error associated with large wakes prompts use of the outflow boundary condition (Gresho & Sani 1998): the outer boundary condition is $\boldsymbol{u} = \dot{\gamma} y \boldsymbol{e}_x$ at the box boundary, except on the portions of the domain which would be outflow surfaces in the undisturbed flow (for example, the portion of one end of the box where $x > 0$ and $y > 0$) where we set $(\nabla \boldsymbol{u} - p\boldsymbol{I}) \cdot \boldsymbol{n} = 0$ with $\boldsymbol{n}$ the normal to this surface. This is described further in §3.3.

2.4. *Validation of flow solver: non-isotropic bodies in shear flow*

The numerical algorithms were thoroughly tested against a variety of known results. In order to evaluate the performance at finite *Re* in the flow of interest, we first compare with analytical results for the torque on a prolate spheroid in Stokes shear flow, and then confirm and extend recent results showing the existence in simple shear of steady finite-*Re* torque-free states for elliptical cylinders and oblate spheroids.

Analytical results for the torque at zero *Re* on a spheroid fixed in simple shear (Kim & Karrila 1991) were used for the case of a prolate spheroid aligned with its long axis along the vorticity direction. The prolate spheroid surface is defined by $x^2/b^2 + y^2/b^2 + z^2/a^2 = 1$, with $a > b$. Calculations were performed on a prolate spheroidal annulus with outer dimension in the plane of shear $R^\infty = 5b$, and the annular volume was discretized using structured tetrahedral meshes in prolate spheroidal coordinates (Moon & Spencer 1971) as discussed in §2.3. Agreement was excellent for $a/b = 1$ to $a/b = 5$, as illustrated by figure 2.

Computed results were obtained for finite-*Re* flow around elliptical cylinders and oblate spheroids at varying angles of inclination, ϕ, from the positive *x*-axis in the (x, y) plane. For both bodies, $\phi > 0$ when measured in a counterclockwise direction. The elliptical cylinder surface with $\phi = 0$ is defined by $x^2/a^2 + y^2/b^2 = 1$, with $a/b > 1$
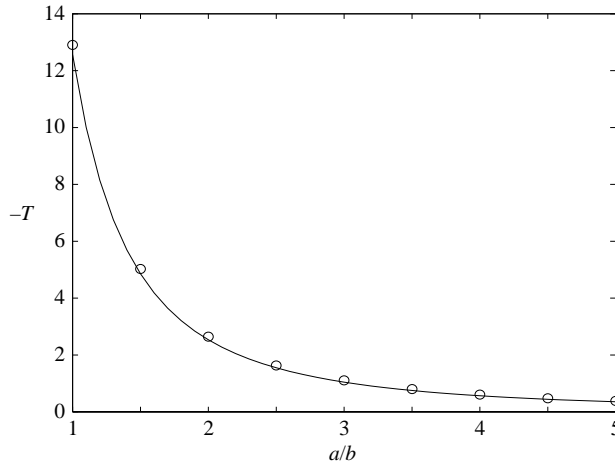
FIGURE 2. Computed (symbols) and analytical (line; Kim & Karrila 1991) torque at $Re = 0$ on prolate spheroids of aspect ratio a/b in simple shear flow. The major axis of the body is aligned with vorticity of the undisturbed flow. The torque, T, is scaled by $a^3 \mu \dot{\gamma}$.

here. Meshing of the fluid volume was performed using unstructured triangular meshes in a box-bounded domain with $H = 5a$ and $L = 25a$. The oblate spheroid surface with $\phi = 0$ is defined by $x^2/a^2 + y^2/b^2 + z^2/a^2 = 1$, with $a > b$. The Reynolds number characterizing the flow is defined in terms of the long axis, $Re = \dot{\gamma} a^2/\nu$. Meshing of the oblate spheroidal annular fluid volume (of $R^\infty = 5b$) was with structured tetrahedral meshes in an oblate spheroidal coordinate system (Moon & Spencer 1971). Recall that, in either case, return to simple shear flow was imposed at the outer boundary.

Lattice-Boltzmann equation solutions of the flow (Aidun, Lu & Ding 1998) found torque-free steady states for simple shear flow around oblate spheroids and elliptical cylinders, and this has been confirmed experimentally for elliptical cylinders by Zettner & Yoda (2001b). Our results agree with these findings, both validating our numerical approach at finite Re and extending the known steady states for these non-isotropic bodies in shear flows.

The torque-free and freely suspended body undergoes a time-dependent motion in the general case, with this motion a Jeffrey orbit at $Re = 0$. For our steady-flow solver, it is thus convenient to seek torque-free steady states at finite Re by fixing the body at a given inclination angle, ϕ, relative to the direction of the undisturbed shear flow, with ϕ measured counterclockwise from the flow direction. The torque for an elliptical cylinder of $a/b = 1.25$ fixed at varying angles of inclination $-\pi/2 < \phi < \pi/2$ is shown for $Re = 0$, 43 and 50 in figure 3(a), showing a single torque-free state at $\alpha \doteq 0.05\pi$ (9°) at $Re = 43$. For $Re < 43$, the torque is always negative (clockwise), while for $R > 43$, there exist two zero-torque positions, of which one is stable as discussed below. There exists a minimum Reynolds number at which a torque-free state is first observed, termed Re^{cr} and for the case $a/b = 1.25$ having value $Re^{cr} \doteq 43$, for which these two zero-torque orientations coalesce to a single value, and this angle is plotted as a function of a/b in figure 3(b). The data points are labelled with a triplet $(a/b, Re^{cr}, \phi^{cr})$ indicating the conditions, where ϕ^{cr} is the inclination angle at which the torque vanishes. Note that $\phi^{cr} < 11.7°$ in the range studied, but does not vary monotonically with a/b. The implications of the torque on the elliptic cylinder in shear have been considered by Ding & Aidun (2000); these authors have found that
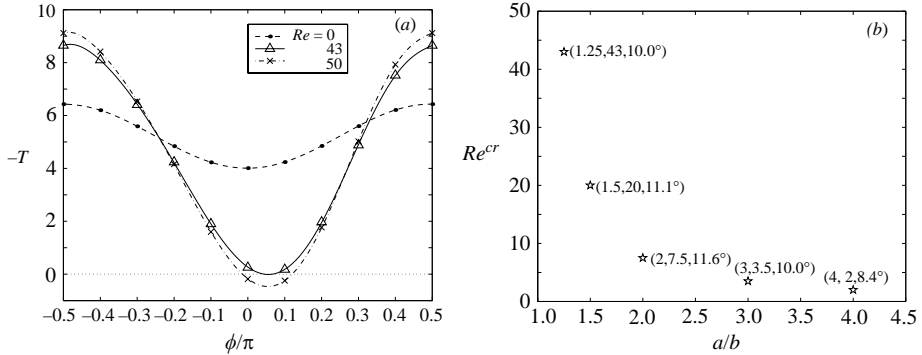
FIGURE 3. (a) Torque per unit length, scaled by $a^2\mu\dot{\gamma}$, on fixed elliptical cylinder of $a/b = 1.25$ as a function of inclination angle, ϕ, relative to the shear flow direction at $Re = 0$, 43 and 50 showing torque-free states for the non-zero Re. (b) Minimum Re at which a torque-free steady flow is observed for simple shear about an elliptical cylinder of varying aspect ratio a/b. Points are labelled with the triplet (Re^{cr}, a/b, ϕ^{cr}) giving conditions at the first point, for increasing Re, of vanishing torque.

above Re^{cr} the system exhibits a saddle-node bifurcation, and that the scaling of the period of rotation, τ, for $Re < Re^{cr}$ as $\tau \sim C(Re^{cr} - Re)^{-1/2}$ with C independent of Re is thus a universal property owing to the behaviour near any saddle node. Similar to Ding & Aidun, we may assess the stability of the two torque-free points for $Re = 50$ and $a/b = 1.25$, representative of a general condition with $Re > Re^{cr}$. Labelling the zeros of the $Re = 50$ curve from left to right as ϕ_1 and ϕ_2, the zero $\phi_2 \approx 0.1\pi$ represents the stable position for this body, as a perturbation to smaller angle carries it into a region where the torque is positive ($-T < 0$ in the figure) and it would be driven back toward ϕ_2. Analysis of this same portion of the curve indicates that a positive perturbation away from ϕ_1 would thus carry the system along the small arc of the curve for which $-T < 0$ to ϕ_2, whereas a perturbation to $\phi < \phi_1$ (left of ϕ_1) brings the system to a negative torque, which would drive a further decrease in ϕ and passage to the stable ϕ_2 from the opposite direction.

Our results agree well with available experimental and numerical results for the elliptical cylinder. Consistent with the trends discussed by Zettner & Yoda (2001*b*), Re^{cr} apparently diverges as a/b approaches unity, and decreases as a/b increases. At $a/b = 2$, we find $Re^{cr} \doteq 7.5$, in good agreement with the value of $Re^{cr} = 7.25$ reported by Ding & Aidun (2000). In figure 4(*a*), the flow pattern for the critical state of an elliptical cylinder of $a/b = 4$, with $Re^{cr} = 2$ and $\phi^{cr} = 8.4°$, is illustrated. Flow reversal zones comparable to those of a sphere with radius equal to the minor axis b, which will be considered further in the following section, are a prominent feature of all of these torque-free states. Note that a closed streamline region, which must exist in the rotating case, is absent.

Torque-free steady flows were also found in limited studies of the oblate spheroid with its minor axis lying on the (x, y) plane. These were found to agree with the results of Ding & Aidun (2000) obtained by the lattice-Boltzmann technique. For example, Ding & Aidun found the torque-free condition of $Re^{cr} \approx 20.25$ at $a/b = 2$, and we find $Re^{cr} = 21$. The angle of inclination, $\phi^{cr} = 18°$, is larger than for the same aspect ratio elliptical cylinder, for which figure 3(*b*) shows the value to be $\phi^{cr} = 11.6°$ at $a/b = 2$. Streamlines and body inclination are illustrated for this condition in figure 4(*b*).
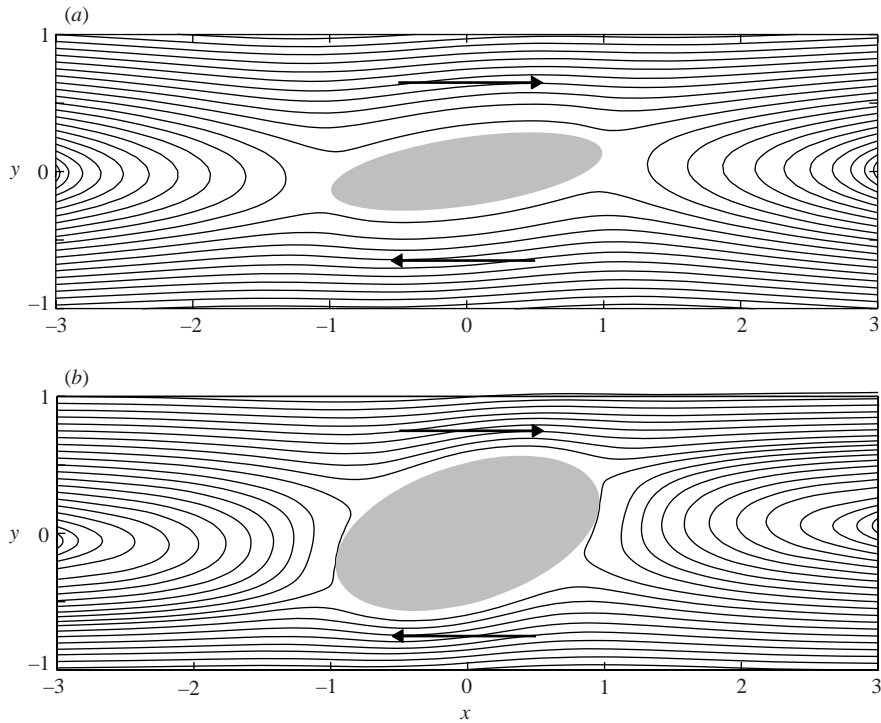
(a)

(b)

FIGURE 4. Body inclination and steady-flow streamlines in simple shear about stationary torque-free bodies: (a) elliptical cylinder at $Re^{cr} = 2$, $a/b = 4$ and $\phi^{cr} = 8.4°$; (b) oblate spheroid, with minor axis on the shear-velocity gradient plane, at $Re^{cr} = 21$, $a/b = 2$ and $\phi^{cr} = 18°$.

3. Simple shear flow around cylinder and sphere at varying Re

The flows caused by a cylinder and sphere in simple shear over a range of Reynolds number have been computed. The flows caused by the different immersed objects have certain similarities, but the sphere causes a considerably more complex flow pattern. We begin in §3.1 by considering the Stokes-flow and inviscid limits for fixed and free bodies. This is followed in §3.2 by study of the flow at weak to moderate inertia, primarily around freely rotating bodies. We then describe the results for strong inertial shear flow for both fixed and free bodies in §3.3; these include observation of separation in these flows.

3.1. *Limiting behaviour: Stokes- and inviscid-flow solutions*

The flows due to simple shear flow around a cylinder or sphere at $Re \equiv 0$ are analytically known for both the fixed and free cases, and the streamlines in the vicinity of the bodies from this condition provide an important baseline for comparison with results at finite Re. The streamlines are shown in figure 5. Unlike the case for uniform flow past a body in two dimensions, there is no net force on the cylinder here and thus there exists a solution for the Stokes flow. The relevant formulae can be described in a single form for both fixed and free bodies by considering a general rotation rate of the body. For the cylinder, these are

$$\left.\begin{aligned} u_x &= \tfrac{1}{2}y(1 - r^{-4}) + \tfrac{1}{2}y(1 - r^{-2}) - 2x^2y(r^{-4} - r^{-6}) - \frac{\Omega y}{r^2}, \\ u_y &= \tfrac{1}{2}x(1 - r^{-4}) - \tfrac{1}{2}x(1 - r^{-2}) - 2xy^2(r^{-4} - r^{-6}) + \frac{\Omega x}{r^2}, \end{aligned}\right\} \tag{11}$$
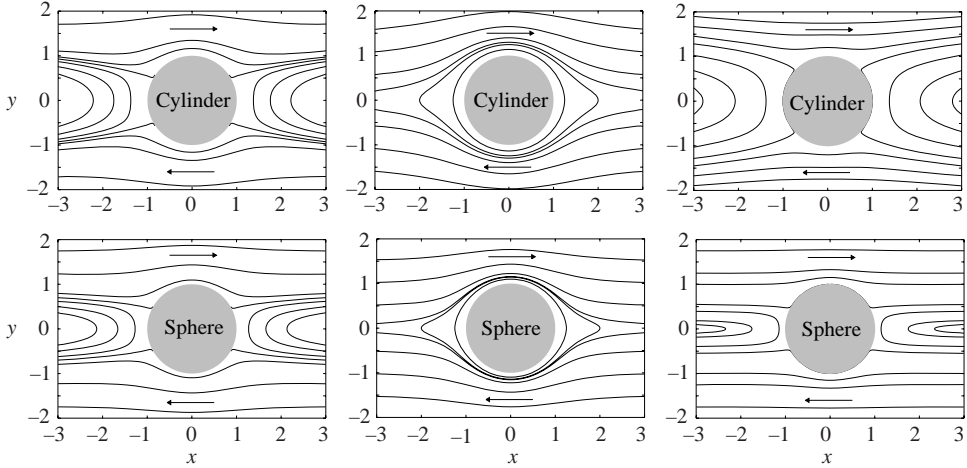
FIGURE 5. Streamlines from the analytical solutions for simple shear flow about bodies in the Stokes flow under fixed and free conditions, and potential flow (left to right, respectively, for the three conditions) for a cylinder in the upper row and sphere in the lower row.

and for the sphere,

$$
\left.\begin{aligned}
u_x &= \tfrac{1}{2}y(1 - r^{-5}) + \tfrac{1}{2}y(1 - r^{-3}) - \tfrac{5}{2}x^2 y(r^{-5} - r^{-7}) - \frac{\Omega y}{r^3}, \\
u_y &= \tfrac{1}{2}x(1 - r^{-5}) - \tfrac{1}{2}x(1 - r^{-3}) - \tfrac{5}{2}xy^2(r^{-5} - r^{-7}) + \frac{\Omega x}{r^3}, \\
u_z &= -\tfrac{5}{2}xyz(r^{-5} - r^{-7}).
\end{aligned}\right\}
\tag{12}
$$

The rotation of either body when torque-free is with angular velocity equal to the undisturbed fluid vorticity, or $\Omega = 1/2$ in the scaling used here.

There are obvious qualitative differences evident at $Re = 0$ for the flow of viscous fluid around a fixed body relative to that about a freely suspended and rotating body. For the freely suspended case, rotation is accompanied, for any Re, by a region of closed streamlines with inner boundary on the body; for $Re = 0$, this region is known to extend infinitely in the flow direction for the circular cylinder (Kossack & Acrivos 1974), and to infinity in the flow and vorticity directions of the driving shear flow for the sphere. For a fixed body at $Re = 0$, reverse flow regions exist, in which fluid which comes from $(x < 0, y > 0)$ reverses direction near the $y = 0$ plane and recedes from the body into the quadrant $(x < 0, y < 0)$.

Flow reversal of this general form is also seen for shear flow in the limit of inviscid flow for two dimensions, where $\Omega = 0$ owing to the lack of surface tractions; the inviscid flow solution for shear flow about a circular cylinder is given by Kossack & Acrivos (1974):

$$
u_x = y - \tfrac{1}{2}y(r^{-2} + r^{-4}) - \frac{(x^2 - y^2)y}{r^6}, \quad u_y = \tfrac{1}{2}x(r^{-2} - r^{-4}) + \frac{(x^2 - y^2)x}{r^6}.
\tag{13}
$$

For the sphere, the irrotational (potential) flow solution satisfying vanishing normal velocity at the surface of the body is given by

$$
u_x = y + \frac{y}{3r^5} - \frac{5}{3}\frac{x^2 y}{r^7}, \quad u_y = \frac{x}{3r^5} - \frac{5}{3}\frac{xy^2}{r^7}, \quad u_z = -\frac{5}{3}\frac{xyz}{r^7},
\tag{14}
$$

but it should be noted that this is not a solution of the inviscid equations for three-dimensional flow, because $\boldsymbol{u} \cdot \nabla \boldsymbol{u} \neq 0$ and the undisturbed vortex lines are, in fact, turned into the streamwise direction and stretched in passage around a sphere; the role of this irrotational solution in developing a lift force and its short-time evolution is considered in Legendre & Magnaudet (1998). We have included this result only to emphasize the similarity in limiting-flow structures for the cylinder and sphere (on the plane of shear). Streamlines from these flow solutions in the vicinity of the bodies are also presented in figure 5. The limiting solutions indicate that for a fixed body it must be expected that, regardless of Re, there will be reversed flow zones in simple shear. For rotating bodies, the limiting $Re = 0$ and inviscid cases suggest the observed behaviour: the closed streamline region collapses and the body rotates progressively more slowly relative to the undisturbed vorticity as Re increases, while the reverse flow regions approach the body at large Re. The influence of viscosity results in a boundary layer on the body surface and separated flow occurs for both the cylinder and sphere. While the behaviour demonstrated by the large-Re solutions may not be experimentally realizable, the results may have theoretical relevance and are in the spirit of the large-Re_U solutions for uniform flow past a cylinder and sphere by Fornberg (1985, 1988, respectively).

3.2. *Moderate fluid inertia*: $0 < Re \leqslant 10$

As Re is increased from zero, the influence of inertia for a fixed cylinder or sphere is not readily apparent from comparison of the streamlines of the flow with its Stokes-flow counterpart, a point which may be rationalized from the similarity of the inviscid streamlines with those in Stokes flow about the fixed bodies. Hence, for these lower Reynolds numbers, we consider only flow about freely rotating bodies.

By contrast to the case of the fixed bodies, the difference in topology of the Stokes and inviscid streamlines about freely rotating bodies is reflected in a dramatic change of the streamlines of finite-Re flow about these bodies. This is true even for relatively weak inertia, and is demonstrated by the collapse of the closed streamline region. This is illustrated by figure 6: the limiting closed streamlines for $Re = 0.1$, 1 and 10 are shown in (a) and (b) for the circular cylinder and sphere, respectively; the points at which the limiting closed streamlines cross the $y = 0$ plane for the sphere under the same conditions in (c) show the rapidity of the collapse in all directions. Limiting streamlines are presented for $R^\infty = 150$ for both the cylinder and the sphere, and are not sensibly changed by further increase in R^∞.

The extent of the closed streamline region may also be assessed by the distance from the centre of the body to the stagnation point between the closed streamlines and the reverse flow. Comparison of the results with the theory in its region of validity, $Re \ll 1$, based on the asymptotic analysis of Poe & Acrivos (1975), is shown in figures 7(a) and 7(b) for the cylinder and for the sphere, respectively. These results agree satisfactorily with the theory provided the outer boundary R^∞ is sufficiently large that the reverse flow regions are not significantly affected. Results for both geometries at $Re \ll 1$, where the stagnation point moves far from the body according to theory, show outer boundary influence at $R^\infty = 10$, as the distance to the stagnation point is reduced well below the theoretical value approached in larger domains. Deviation from the theory even for convergence with respect to R^∞ for the sphere occurs at $Re \approx 10^{-2}$ rather than $Re \approx 10^{-1}$ for the cylinder, a result which may be influenced by the coarser mesh used for the sphere.

The three-dimensional streamline structure near the sphere is shown in figure 8 for $Re = 0$, 1 and 10. In figure 9, the disturbance streamlines on the shear plane are shown
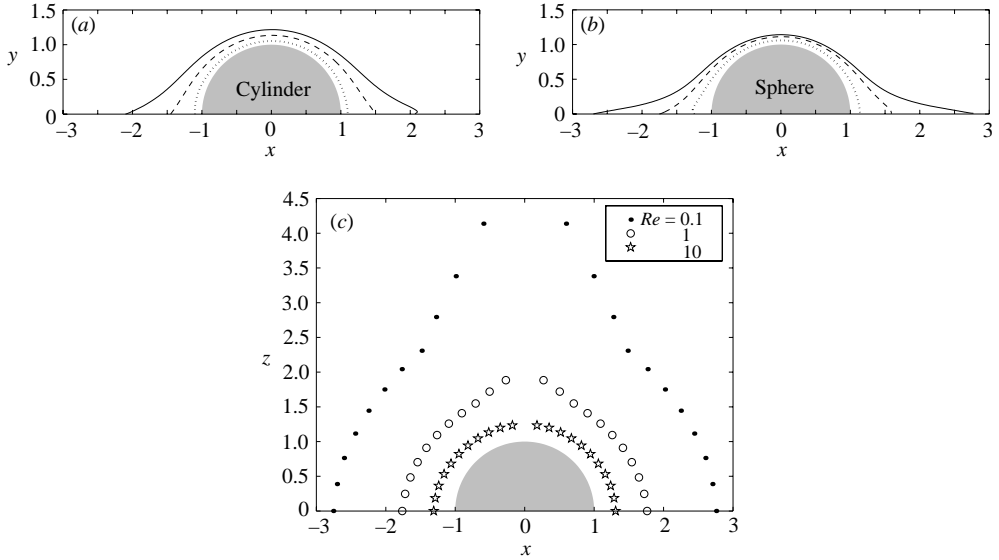
FIGURE 6. Limiting closed streamlines for torque-free bodies in simple shear flow ($u_x = y$) about the (*a*) circular cylinder and (*b*) sphere in the plane of shear at $Re = 0.1$ (solid line), 1 (dashed) and 10 (dotted). In (*c*) are the points where the limiting closed streamlines cross $y = 0$ in the case of the sphere.
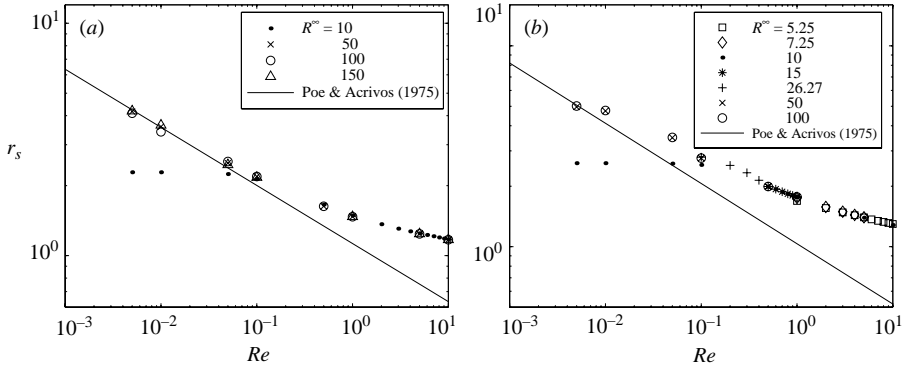

FIGURE 7. The distance, measured from the centre of the body, to the stagnation point separating closed streamlines and reverse flow: (*a*) circular cylinder and (*b*) sphere. The results are presented for a range of outer boundary distances R^∞, with the asymptotic prediction at $Re \ll 1$ of Poe & Acrivos (1975) shown as a solid line.
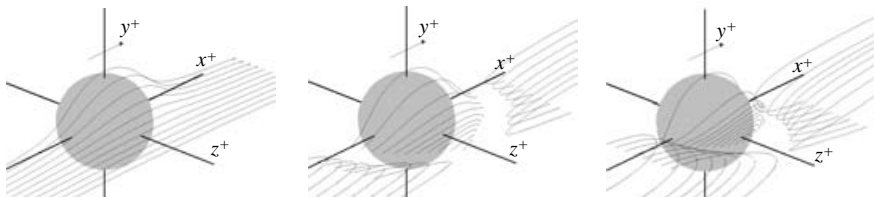

FIGURE 8. Streamlines near the torque-free sphere at $Re = 0$, 1 and 10 (left to right).
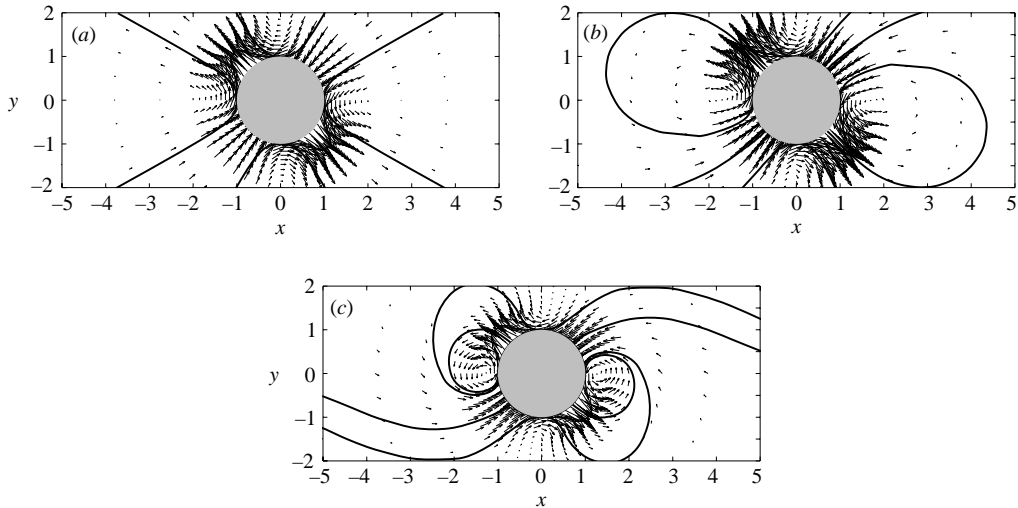
FIGURE 9. Streamlines and velocity vectors of the disturbance flow caused by a torque-free sphere in simple shear flow for (*a*) $Re = 0$, (*b*) $Re = 1$ and (*c*) $Re = 10$.

for a sphere, also at $Re = 0$, 1 and 10. The disturbance is found by taking the complete velocity and subtracting the undisturbed shear flow, i.e. we present $\boldsymbol{u}' = \boldsymbol{u} - \boldsymbol{u}^\infty$. The streamlines shown then follow the definition of being locally tangent to the velocity vector, here $\boldsymbol{u}'$, and the relative magnitude of the disturbance field is illustrated by presenting vectors of $\boldsymbol{u}'$; the scale of these vectors follows by noting that they have magnitude of $|\boldsymbol{u}'| \approx 1$ (dimensional form $|\boldsymbol{u}'| \approx \dot{\gamma} a$) on the surface of the sphere at $x = \pm 1$. A notable feature is that at $Re = 0$, the particle introduces a flow parallel in form but opposite in direction to the extensional component of $\boldsymbol{u}^\infty$, while at $Re = 1$ and 10, the disturbance flow rather evidently contains significant vorticity.

The surface traction vector, which will be denoted $\boldsymbol{t}$, is given by $\boldsymbol{t} \equiv \boldsymbol{\sigma} \cdot \boldsymbol{n}$ evaluated from the fluid stress $\boldsymbol{\sigma}$ at the surface of the body, with surface normal $\boldsymbol{n}$ projecting into the fluid. The surface traction vector has component normal to the surface $(\boldsymbol{n} \cdot \boldsymbol{\sigma} \cdot \boldsymbol{n})$ and a component tangential to the surface ('shear' component) and thus lying in the plane perpendicular to $\boldsymbol{n}$. For a cylinder, these are readily visualized in a standard x–y plot. The same is true of the equivalent stress components on the surface of a sphere on the shear plane ($z = 0$). In figure 10, for $Re = 0$, 1 and 10, the normal stresses on a cylinder are plotted in (*a*) and on the shear plane for a sphere in (*b*). The tangential stress at these Re for a cylinder and sphere appear in figures 10(*c*) and 10(*d*), respectively. The shape of the curves for cylinder and sphere and direction of deviation from the Stokes-flow result at finite Re are seen to be quite similar; although the magnitude of deviation from Stokes-flow results are similar for the normal stress, the shear stress deviation is significantly smaller for the sphere.

3.3. *Strong fluid inertia: $Re > 10$*

To probe flow behaviour as $Re \to \infty$, we alter the computational approach detailed in §2, for which we observe that the number of iterations required for the iterative solver to achieve an acceptable level of convergence increases with Re and with the size of the computed domain. The success of Newton's method used by the direct solver is also negatively influenced by the domain size. The end result is that computations for $Re > 10$ were found to be impractical for the large domains required in simulating unbounded flows. To study the flow development near the bodies at $Re \gg 1$, we
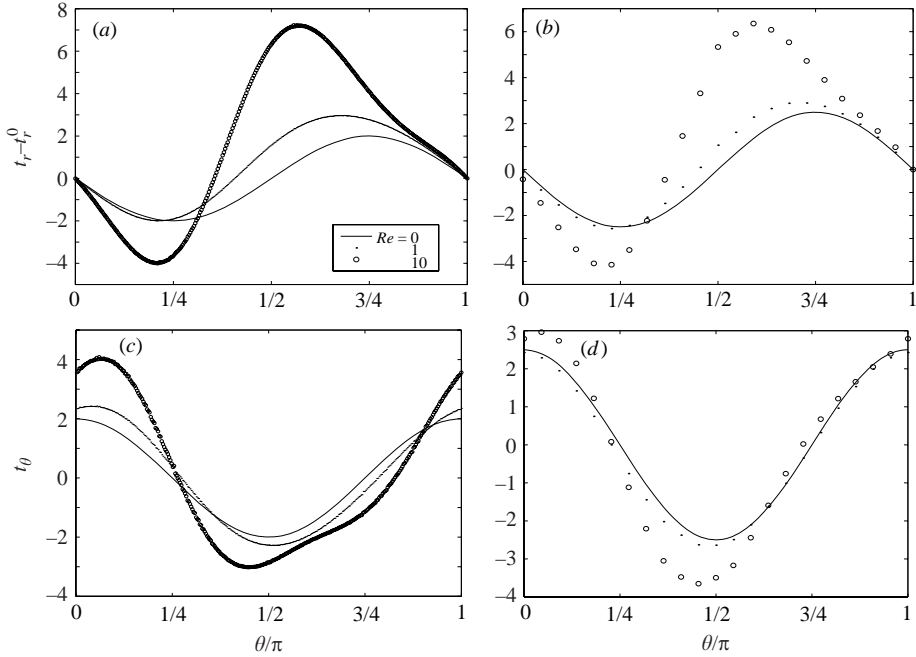
FIGURE 10. For zero and moderate Re, normal tractions for (a) cylinder and (b) sphere on the shear plane, and tangential tractions for (c) cylinder and (d) sphere in plane of shear. The stresses are scaled by $\mu\dot{\gamma}$.

have designed the following numerical experiment applied to flow past a cylinder or a sphere. The particle is centred within a channel with boundaries at $x = \pm L$, $y = \pm H$, and for a sphere at $z = \pm W$. We limit the size of our domain so that $W = H = 2a$ and $L = 5a$ (this maintains the channel Re at values which were found to remain stable). The boundary condition of return to simple shear flow, $\boldsymbol{u} = \dot{\gamma} y \boldsymbol{e}_x$, generates the most error for downstream boundaries since high-Re flows generally produce wakes that stretch to large distances in the streamwise direction. On these downstream boundaries, i.e. $x = L$, $y > 0$ and $x = -L$, $y < 0$, we use the outflow boundary condition, $(\nabla \boldsymbol{u} - p\boldsymbol{I}) \cdot \boldsymbol{n} = 0$, recommended by Gresho & Sani (1998), with a condition of return to shear flow on all other boundaries. Because the conditions simulated are restrictive, we present only results associated with near-body flows.

Considering first the cylinder, the streamlines for flow at $10 < Re < 85$ are qualitatively similar to those shown for $Re = 10$ illustrated in the preceding section. However, for $Re > 85$ there is a qualitative change near the body as boundary-layer separation is observed for the fixed cylinder, as illustrated for $Re = 100$ and 500 in figures 11(a) and 11(b), respectively. At sufficiently elevated Re, the streamlines around the fixed and freely rotating body become essentially indistinguishable, even in the separation region, as the closed streamlines are compressed extremely near the body. This is illustrated by comparing the streamlines for the fixed and freely rotating condition at $Re = 500$ in figures 11(b) and 11(c), respectively. The development from conditions near the critical Re for separation to a dual vortex structure at elevated Re is demonstrated by the close views of the separation (wake) region in figure 11 at $Re = 100$, 200 and 500 for the fixed cylinder, as well as for the torque-free rotating case at $Re = 500$. Figures 11 and 12 illustrate the very slight dependence on the surface condition of the flow away from the body.
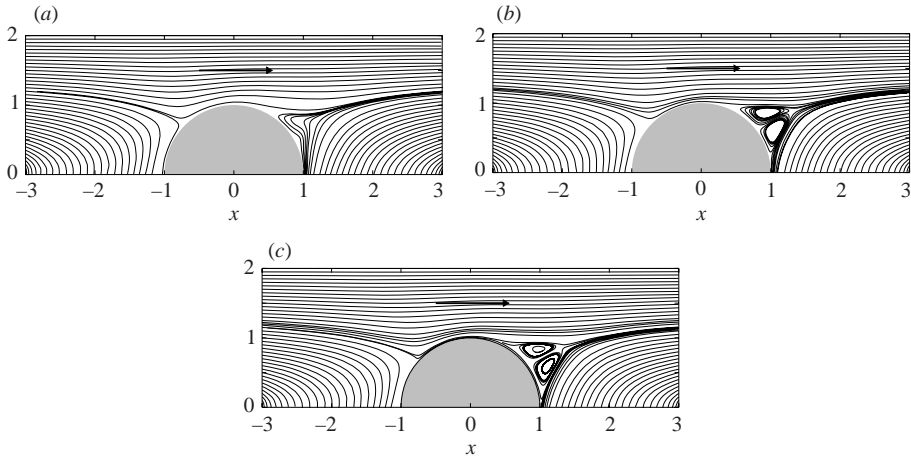
FIGURE 11. Streamlines for imposed simple shear $u_x = \dot{\gamma} y$ (arrows show direction) around a circular cylinder for (*a*) $Re = 100$, fixed; (*b*) $Re = 500$, fixed; and (*c*) $Re = 500$, torque-free (freely rotating).
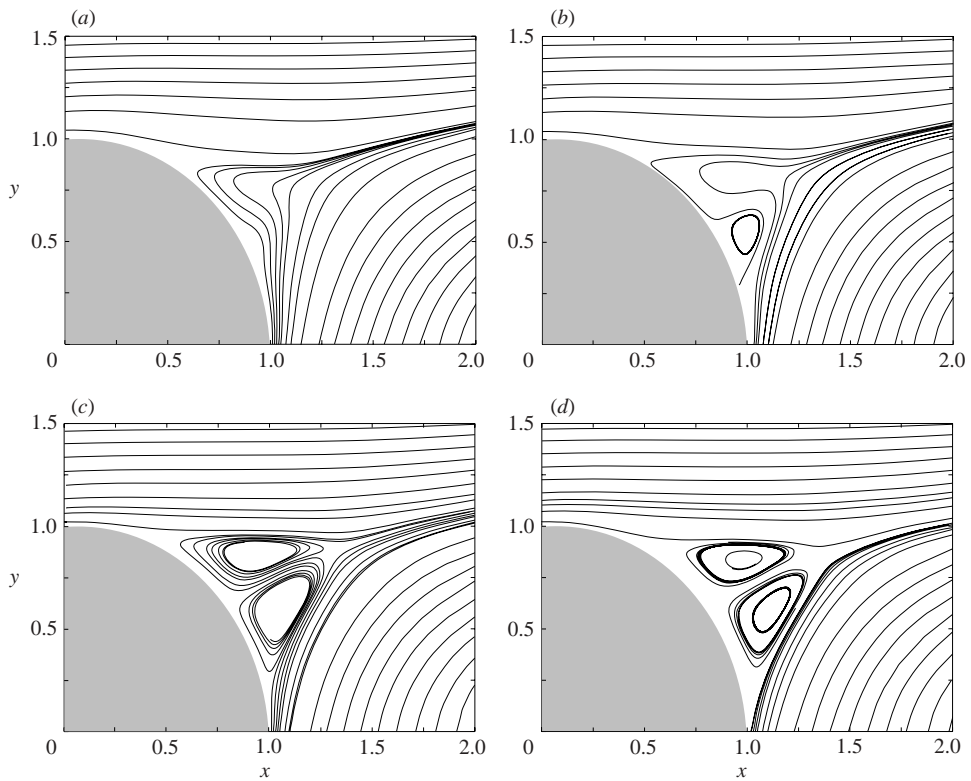

FIGURE 12. Close views of streamlines in the separation zone for imposed simple shear $u_x = \dot{\gamma} y$ around a cylinder for (*a*) $Re = 100$, fixed; (*b*) $Re = 200$, fixed; (*c*) $Re = 500$, fixed; and (*d*) $Re = 500$, torque-free (freely rotating).
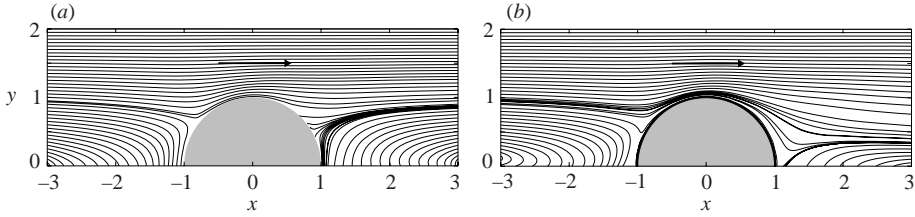
FIGURE 13. Streamlines at $Re = 100$ for (a) a fixed sphere and (b) a torque-free (freely rotating) sphere. Direction of the imposed shear flow $u_x = \dot{\gamma} y$ is indicated by the arrows.
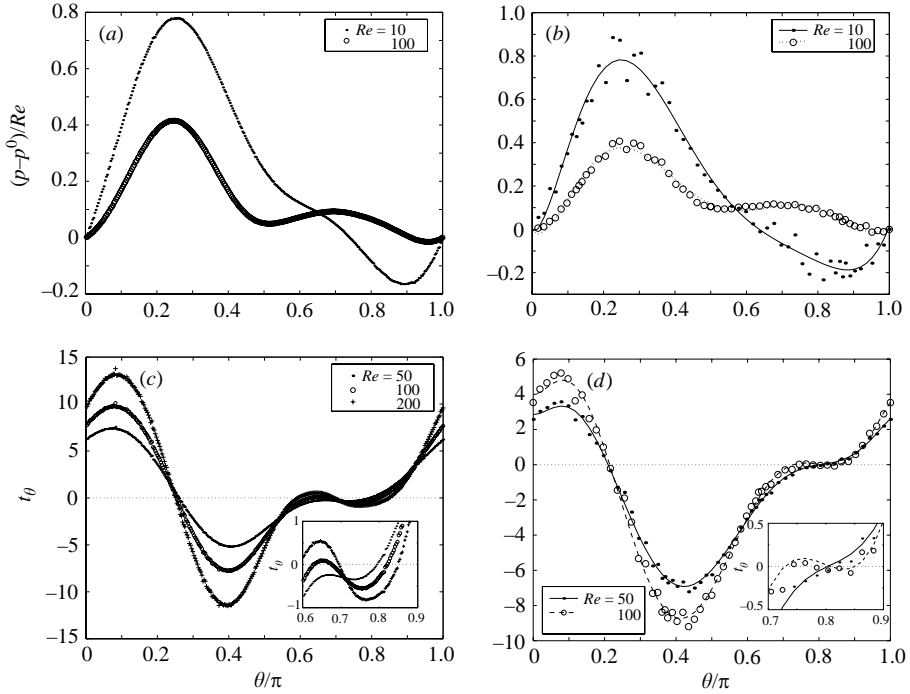

FIGURE 14. Surface tractions computed in the box domain used for elevated Re. Surface pressure, scaled by $\mu \dot{\gamma} Re = \rho \dot{\gamma}^2 a^2$, shown in (a) for the cylinder and in (b) for shear plane of the sphere. Tangential tractions, scaled by $\mu \dot{\gamma}$, are shown in (c) for the cylinder and in (d) for the sphere.

In figure 13(a), streamlines in shear flow about the fixed sphere at $Re = 100$ are illustrated. These show a zone of streamlines in the range $\pi/8 < \phi < \pi/4$ which appear to emanate from multiple stagnation points on the downstream side of the sphere, indicative of separation and confirmed by the traction data described below. We find $Re \approx 100$ is very near the lower limit of Re for the observation of this behaviour for spherical particles in the domain used for computation, but have not sought the precise value because of the potential limitations placed on general validity by the small domain.

At sufficiently elevated Re, the streamlines provide clear evidence of separation, as shown for the cylinder in figure 11, but the situation is less clear near the onset of the phenomenon. Surface tractions provide a clearer guide, and surface tractions for the cylinder and shear plane of a sphere are shown in figure 14 as a function of the
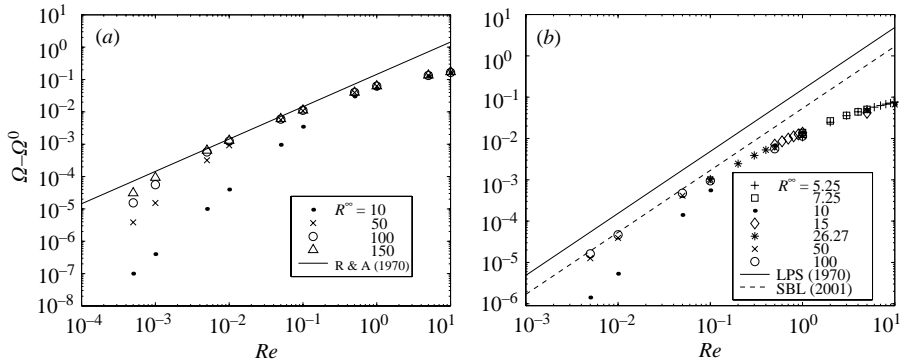
FIGURE 15. Rotation rate deviation from zero-Re value for (a) cylinder (curve from Robertson & Acrivos 1970) and (b) sphere (curves from Lin *et al.* 1970 and Stone *et al.* 2001).

angle θ defined positive clockwise from $\theta = 0$ on the negative x-axis. Caution must be exercised because the Re of onset of separation may be influenced by the near boundary of the domain. We consider first the excess pressure, in figures 14(a) and 14(b). Results for the sphere are found to be noisier in this domain with unstructured mesh, and a smooth curve fitted to the data appears along with the actual computed values. The pressure is of similar form to the normal traction in figure 10, but is of opposite sign owing to the standard convention of writing the isotropic portion of the stress as $-p\boldsymbol{I}$. The pressure is considered here because of the accepted role of pressure gradients along the surface in determining separation. We see that at $Re = 10$, the pressure curves for cylinder or sphere are very similar, with the excess pressure continuously decreasing downstream of the point $\theta = \pi/2$, and no separation is observed here. At $Re = 100$, the excess pressure is positive over all angles for either the surface of the cylinder or the shear plane of the sphere, but undergoes non-monotonic variation downstream of $\theta = \pi/2$. In figure 14(c), illustrating the tangential traction component for the cylinder, the form of the curve evidences separation at $Re = 100$ and 200, but not at $Re = 50$, indicating onset in the range $50 < Re < 100$; the inset shows the stress on a magnified scale. Specifically, we take the non-monotonic variation of the tangential traction in conjunction with its local maxima and minima of opposite sign on the 'downstream' portion of the surface, $\pi/2 < \theta < \pi$, as indicative of separation. The first appearance of separation based on this definition is found at $Re \approx 85$. For the sphere, figure 14(d) shows the tangential traction curve at $Re = 100$ is nearly flat in this region, but the inset shows three closely spaced zeros.

4. Rotation rate and stresslet

4.1. *Variation of rotation rate with Re*

For the torque-free isotropic bodies, the rotation rate is determined as part of the flow solution, by the approach outlined in §2. Either body has a rotation rate at $Re = 0$ equal to the fluid vorticity, or $\Omega_0 = -1/2$, and whose magnitude decreases with increasing Re. The difference $\Omega - \Omega_0$ is plotted along with the theoretical result appropriate to the geometry of the body, in figure 15(a) for the cylinder and in figure 15(b) for the sphere. The zero-Re values of rotation rate computed for the cylinder are within 0.2% of the theoretical value of $\Omega_0 = -1/2$ for $R^\infty > 10$ (and always of slightly larger magnitude), while table 1 shows the computed values of Ω_0 to be within 0.1% of the theoretical value for the sphere. The agreement with theory

R^∞	Ω^0	S_{12}^0
10	−0.4996	11.043
50	−0.4996	10.962
100	−0.4996	10.961
300	−0.4996	10.961
1000	−0.4996	10.961

TABLE 1. Computed $Re = 0$ values for the sphere rotation rate and shear component of the stresslet.
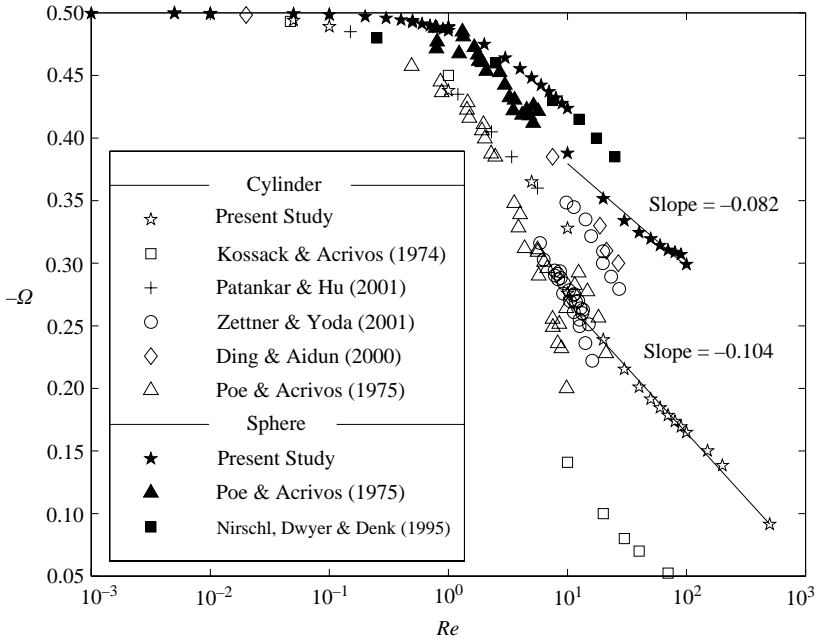

FIGURE 16. Rotation rates of the freely suspended circular cylinder and sphere in simple shear flow computed in this work along with results from other numerical and experimental studies.

of Robertson & Acrivos (1970) who found $\Omega = -1/2 + 0.1443 Re$ is good for the cylinder at $Re < 0.1$ for sufficiently large outer radius of the domain, with $R^\infty = 150$ being sufficient for $10^{-3} < Re < 10^{-1}$. Deviation from the theory begins at $Re > 0.1$. For the sphere, we find almost perfect agreement with the theory of Stone *et al.* (2001) for $0.005 < Re < 0.05$ for $R^\infty = 100$, and deviation from the theory is judged to be significant for $Re > 0.1$. The slope of the theory of Lin *et al.* (1970) is identical, but is offset from our results by a constant factor of approximately 3: the theories predict $\Omega_{LPS} = -1/2 + 0.0535 Re^{3/2}$ and $\Omega_{SBL} = -1/2 + 0.1538 Re^{3/2}$, and our results agree closely with Ω_{SBL}. In figure 16, the torque-free cylinder and sphere rotation rates computed in this work are plotted with the results of other finite-Re numerical and experimental studies. Here, the reduction in $|\Omega|$ is seen to be generally smaller for the sphere, primarily because of the weaker dependence on Re of the deviation from Ω_0 in the asymptotic theories noted above, $O(Re^{3/2})$ for the sphere and $O(Re)$ for the cylinder. At large Re, the decrease of $|\Omega|$ for sphere and cylinder with Re is very similar as seen by the slope drawn for this portion of our data. The difference between

the Ω values for either body determined using the two computational domains at $Re = 10$, with the wall-bounded (box) domain value significantly lower than that in the annular domain, suggests strong boundary effects for the box domain for either a cylinder or sphere. Such boundary effects appear in the experimental results as well: the appearance of more than one trend line in data from experimental studies indicates different ratios of the body size to shear-flow gap (a/H) and the reader is referred to the references for complete details. Our results are generally consistent with the trend previously illustrated by Ding & Aidun (2000) (see their figure 2), specifically that the rotation rate generally is larger, and the magnitude of its negative slope with respect to increasing Re is smaller, for larger a/H. For example, our results for the cylinder at $a/H = 1/2$ in the box domain have larger $|\Omega|$ and weaker slope than do the results of Ding & Aidun at $a/H = 1/4$ and these results in turn have rotation rate larger and slope weaker than the results of Kossack & Acrivos (1974) with $a/H \to 0$. A plausible explanation for this result which has not, to our knowledge, been previously offered is given simply by considering that the limiting case of $a/H = 1$ requires the immersed body to move with the driving boundaries (with which it is in this case in contact), and the results reflect the influence of this condition.

4.2. *Stresslet at finite Re*

For Stokes flow, it is well known that the traction at the surface of the particle can be related to the particle contribution to the bulk stress. By considering a volume or ensemble average of the stress in the suspension, Batchelor (1970) showed that the sum of hydrodynamic stresslets, with the stresslet for a rigid sphere given by

$$S_{ij} = \tfrac{1}{2} \int_{A_p} (x_i \sigma_{jk} + x_j \sigma_{ik}) n_k \, \mathrm{d}A, \tag{15}$$

where A_p represents the sphere surface with n_k the normal from the surface, results in the dilute, or Einstein, viscosity contribution of the particles $\eta(\phi) = \mu(1 + 5\phi/2)$. In general, there are nonhydrodynamic contributions from interparticle forces and Brownian motion as well (Russel, Saville & Schowalter 1989) and these have been considered both analytically for dilute pair interactions (e.g. by Brady & Morris 1997) and for concentrated systems by simulation (Phung, Brady & Bossis 1996). While we consider only hydrodynamic stresses, for a finite-Reynolds-number suspension the stresslet is not the only contribution. In this case, the presence of the convective acceleration, $\boldsymbol{u} \cdot \nabla \boldsymbol{u}$, in the momentum equation, introduces an added mechanism for momentum transport, well-known as a Reynolds stress in turbulent flows, but present in laminar conditions when particles disturb the shear flow. The hydrodynamic particle stress is given by

$$\frac{\boldsymbol{\Sigma}_p}{3\phi/4\pi} = \boldsymbol{S} - Re \frac{1}{2} \int_{V_p} (\boldsymbol{x}\boldsymbol{a} + \boldsymbol{a}\boldsymbol{x}) \, \mathrm{d}V - Re \int_{V_p + V_f} (\boldsymbol{u} - \boldsymbol{u}^{\infty})(\boldsymbol{u} - \boldsymbol{u}^{\infty}) \, \mathrm{d}V, \tag{16}$$

where $\boldsymbol{S}$ is the stresslet given just above, and $\boldsymbol{a}$ represents the local material acceleration. The integral over the particle volume is due to the acceleration of the body (recall that even in steady rotation, the body is constantly under angular acceleration) and the integration over the entire (particle plus fluid) volume has the form of a Reynolds stress. We address here only the first term, the extension of the stresslet to flow at finite Reynolds number about a rigid body.

We present in figure 17 various rheologically interesting quantities resulting from the stresslet on a sphere. These include S_{12} plotted as the difference from the zero-Re
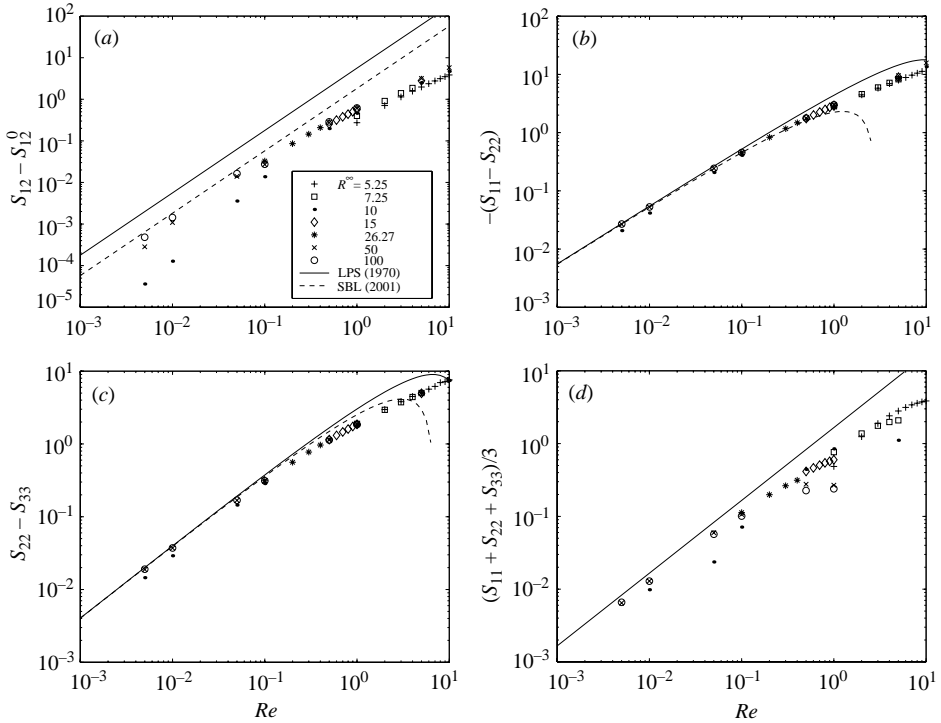
FIGURE 17. Components of the deviation of the stresslet, scaled by $\mu\dot{\gamma}a^3$, from zero-Re values as function of Re: (a) the shear component S_{12}, (b) $S_{11} - S_{22}$, (c) $S_{22} - S_{33}$ and (d) $(S_{11} + S_{22} + S_{33})/3$. The curves are from theories of Lin *et al.* (1970) and Stone *et al.* (2001).

value (computed zero-Re values appear in table 1 and are systematically above the theoretical value of $S_{12,0} = 10\pi/3 \approx 10.47$ by roughly 5%), the first ($S_{11} - S_{22}$) and second ($S_{22} - S_{33}$) normal stress difference contributions, and the trace of the stresslet given by $S_{ii}/3 = (S_{11} + S_{22} + S_{33})/3$. The last is a quantity related to what is termed the 'suspension pressure,' and shown analytically to be zero at $Re = 0$ for a single sphere by Jeffrey, Morris & Brady (1993). Theoretical predictions of both Lin *et al.* (1970) and Stone *et al.* (2001) are plotted along with the computed results. The predictions of Lin *et al.* (1970) are

$$\left. \begin{array}{c} S_{12} = \dfrac{10\pi}{3} + 5.61\,Re^{3/2}, \quad S_{11} - S_{22} = \dfrac{-16\pi}{9}\,Re + 1.202\,Re^{3/2}, \\[2mm] S_{22} - S_{33} = \dfrac{409\pi}{315}\,Re - 1.056\,Re^{3/2}; \end{array} \right\} \quad (17)$$

those of Stone *et al.* (2001) include also the trace of the stresslet and are

$$\left. \begin{array}{c} S_{12} = \dfrac{10\pi}{3} + 1.82\,Re^{3/2}, \quad S_{11} - S_{22} = \dfrac{-16\pi}{9}\,Re + 3.343\,Re^{3/2}, \\[2mm] S_{22} - S_{33} = \dfrac{409\pi}{315}\,Re - 1.558\,Re^{3/2}, \quad \tfrac{1}{3}S_{ii} = \dfrac{19\pi}{36}\,Re. \end{array} \right\} \quad (18)$$

The two theories agree in predicting that the first influence of inertia is to generate finite normal stress effects at $O(Re)$, with the numerical values also in agreement at this level. The theories differ, however, at $O(Re^{3/2})$, as seen previously for the rotation

rate. Our results again agree more closely with Stone *et al.* for S_{12}; agreement of the theories for the leading-order normal stress differences makes a comparison with the numerics for these quantities unclear.

5. Concluding remarks

The problem of simple shear flow around suspended bodies is basic to suspension mechanics, and, in the general case, involves finite inertia, particle interactions and unsteadiness. This work has addressed only a subset of these flows, as we have studied the role of inertia for stationary shear flows around isolated bodies. While we have confirmed and extended results for elliptical cylinders, our examination has focused on flow around the circular cylinder and sphere.

We have observed that introducing weak inertia causes a very rapid collapse of the closed streamline region around freely-rotating bodies. Theory predicts infinitely extended closed streamlines in the flow direction at $Re = 0$; the extent along this axis for the cylinder and sphere is, respectively, 2.2 and 2.8 radii at $Re = 0.1$. Collapse in the vorticity direction for an immersed sphere is similarly rapid. We conclude that the infinite extent of closed streamlines at $Re = 0$ is apparently a singular behaviour, and the streamlines at weak inertia thus cannot be effectively approximated by their Stokes-flow form.

An observation related to the closed streamlines is that the streamlines in simple shear flow about fixed and free bodies, which are qualitatively distinct at $Re = 0$, become progressively more similar as the inertia level increases. The dependence on the motion of the surface is of little consequence away from the body for $Re \geqslant O(1)$. By considering a wall-bounded computational domain, we have extended consideration to $Re \gg 1$, and have observed separation for the fixed cylinder at $Re \approx 85$ and for the fixed sphere at $Re \approx 100$. The presence of closed streamlines orbiting the freely rotating body always contrasts with the immobile fluid contacting the fixed body, yet the stationary flow patterns of fixed and free bodies become essentially indistinguishable – even in the appearance of separation features – when $Re = 100$ or greater. Further increase of inertial influence, to $Re = 500$, for the cylinder leads to predictions of paired standing vortices on the downstream side of the body, for either condition. The physical realizability of these results is unclear, because the steady flow may become unstable.

The strong disturbance caused by the immersed body even at smaller Re has been observed to impact upon the larger-scale flow. This was shown for fixed (but force-free) cylinders and spheres by Bottin *et al.* (1997, 1998), while Matas, Morris & Guazzelli *et al.* (2003) have shown that neutrally buoyant, and presumably on average force-free, suspended spherical particles at dilute conditions lead to laminar–turbulent transition in a pipe at substantially lower pipe Reynolds number than observed for the pure fluid. In the latter of these studies, particle-scale inertia was argued to play a role as pronounced effects of the dilute particles were seen only for $Re = O(1)$. Study of the coupling of the particle scale to bulk scale flows may benefit from results presented here.

The role of inertia upon the stresslet contributions to the bulk suspension stress have been examined for $Re < 10$. Our results confirm the first influence of Re is $O(Re)$ in the normal stresses and $O(Re^{3/2})$ in the shear stress component, consistent with the scaling predicted first for simple shear flow by Lin *et al.* (1970) and later for more general linear flows by Stone *et al.* (2001). We find better, and in fact very good, agreement with the coefficients obtained by Stone *et al.* for these Re-dependent

quantities. Both the computed stress and rotation rate suggest a missing constant factor in the calculations by Lin *et al.* Numerical evaluation of the complete stress, including Reynolds stress contributions, generated by a sphere at finite *Re* is deferred to future work.

Appendix. Direct and iterative solution methods
A.1. *A direct solver for two-dimensional flow*

We use direct methods for solving fluids problems in two dimensions. An application of the finite-element discretization presented above leads to a nonlinear system of algebraic equations, which we convert using Newton's method to a series of linear problems. We use MATLAB's direct sparse solver to solve each resulting system of linear equations.

Rather than discretizing the Navier–Stokes equations and then linearizing the resulting algebraic equations as needed in a Newton iteration, we reverse the order of these two steps. For finite-element or projection type discretizations, the two operations commute so that in the end the same set of equations defining Newton's method result. The starting point for this approach (Holst, Baker & Wang 2000) begins with the weak form of the Navier–Stokes equations written as

$$\langle F(\boldsymbol{u}, p), (\boldsymbol{v}, q)\rangle = \int_{V_f} (\nabla \cdot \boldsymbol{u})q \, \mathrm{d}\boldsymbol{x} + \int_{V_f} \rho[(\boldsymbol{u} \cdot \nabla)\boldsymbol{u}] \cdot \boldsymbol{v} \, \mathrm{d}\boldsymbol{x} + \int_{V_f} \mu \nabla \boldsymbol{u} : \nabla \boldsymbol{v} \, \mathrm{d}\boldsymbol{x}$$
$$- \int_{V_f} p(\nabla \cdot \boldsymbol{v}) \, \mathrm{d}\boldsymbol{x} - \int_{V_f} \boldsymbol{f} \cdot \boldsymbol{v} \, \mathrm{d}\boldsymbol{x} = 0. \qquad (A\,1)$$

We combine the momentum and continuity equations into one weak form (with the restriction that we test separately with q and $\boldsymbol{v}$ to maintain their separate contributions). Written in this way, we think of $\langle F(\cdot), \cdot\rangle$ as a functional of $(\boldsymbol{u}, p)$ and form its variational derivative as

$$\langle DF(\boldsymbol{u}, p)(\boldsymbol{w}, s), (\boldsymbol{v}, q)\rangle = \frac{\mathrm{d}}{\mathrm{d}\epsilon}\langle F(\boldsymbol{u} + \epsilon \boldsymbol{w}, p + \epsilon s), (\boldsymbol{v}, q)\rangle|_{\epsilon=0}, \qquad (A\,2)$$

which when applied to (19) results in

$$\langle DF(\boldsymbol{u}, p)(\boldsymbol{w}, s), (\boldsymbol{v}, q)\rangle = \int_{V_f} (\nabla \cdot \boldsymbol{w})q \, \mathrm{d}\boldsymbol{x} + \int_{V_f} \rho[(\boldsymbol{u} \cdot \nabla)\boldsymbol{w}] \cdot \boldsymbol{v} \, \mathrm{d}\boldsymbol{x}$$
$$+ \int_{V_f} \rho[(\boldsymbol{w} \cdot \nabla)\boldsymbol{u}] \cdot \boldsymbol{v} \, \mathrm{d}\boldsymbol{x} + \int_{V_f} \mu \nabla \boldsymbol{w} : \nabla \boldsymbol{v} \, \mathrm{d}\boldsymbol{x} - \int_{V_f} s(\nabla \cdot \boldsymbol{v}) \, \mathrm{d}\boldsymbol{x}. \qquad (A\,3)$$

In practice, we use the MINI element to discretize (A 1) and (A 3) where $\boldsymbol{w}_h = \sum_{j=1}^{N_N+N_L} \boldsymbol{W}_j \phi_j, s_h = \sum_{j=1}^{N_N} S_j \psi_j$, and we take as test functions $([\phi_i, 0], 0)$ and $([0, \phi_i], 0)$ for $i = 1, \ldots, N_N + N_L$ and $([0, 0], \psi_i)$ for $i = 1, \ldots, N_N$. Given a $(\boldsymbol{u}_h, p_h)$ from either an initial guess or a previous iteration, (A 1) and (A 3) lead to a sparse matrix of size $2(N_N + N_L) + N_N \times 2(N_N + N_L) + N_N$ for $\langle DF(\boldsymbol{u}_h, p_h)(\boldsymbol{w}_h, s_h), (\boldsymbol{v}_h, q_h)\rangle$ and a vector

of length $2(N_N + N_L) + N_N$ for $\langle F(\boldsymbol{u}_h, p_h), (\boldsymbol{v}_h, q_h)\rangle$. These discrete forms are used in the following Newton iteration scheme.

Algorithm 1. Newton's method for the discrete Navier–Stokes equations.
 Given $\boldsymbol{u}_h^0$ and p_h^0, set $k = 0, 1, 2, \ldots$
 1. Compute $\langle F(\boldsymbol{u}_h^k, p_h^k), (\boldsymbol{v}_h, q_h)\rangle$.
 2. Compute $\langle DF(\boldsymbol{u}_h^k, p_h^k)(\boldsymbol{w}_h, s_h), (\boldsymbol{v}_h, q_h)\rangle$.
 3. Compute $\boldsymbol{w}_h$ and s_h such that $\langle DF(\boldsymbol{u}_h^k, p_h^k)(\boldsymbol{w}_h, s_h), (\boldsymbol{v}_h, q_h)\rangle = -\langle F(\boldsymbol{u}_h^k, p_h^k), (\boldsymbol{v}_h, q_h)\rangle, \forall (\boldsymbol{v}_h, q_h)$.
 4. Set $\boldsymbol{u}_h^{k+1} = \boldsymbol{u}_h^k + \boldsymbol{w}_h$ and $p_h^{k+1} = p_h^k + s_h$.
 We use the sparse solver in MATLAB to handle the system of linear equations that arises for each iteration of Newton's method. We iterate until $\|\langle F(\boldsymbol{u}_h^k, p_h^k), (\boldsymbol{v}_h, q_h)\rangle\| < 1.0 \times 10^{-8}$.

A.2. *Iterative solver for the discretized Navier–Stokes problems*

We apply an iterative approach to handle the nonlinearity generated by the discretized Navier–Stokes equations (9). The method is especially attractive for large-scale problems since it simplifies to a sequence of discrete Stokes problems and hence only requires the storage of two sparse matrices. As opposed to a Newton iteration, these matrices only need to be assembled once, not at every iteration. Furthermore, all the linear algebra problems that arise involve symmetric positive definite matrices and are easily solved with conjugate gradient methods. Since this approach has been well documented by Glowinski (1984), we provide only a summary. The approach begins by interpreting the solution of the Navier–Stokes equations as the solution to a minimization problem. Recall the weak formulation of the Navier–Stokes equations (8), taking $\boldsymbol{u} = \boldsymbol{g}$ on Γ. If we automatically require all velocity functions to be weakly divergence-free by introducing the new velocity trial space $\tilde{V}_g = \{\boldsymbol{w} \in V_g, \int_{V_f}(\nabla \cdot \boldsymbol{w})q \, \mathrm{d}\boldsymbol{x} = 0, \ \forall q \in Q\}$ and the corresponding velocity test space $\tilde{V}_0$, this weak formulation is equivalent to

$$\left.\begin{aligned} \int_{V_f} \mu \nabla \boldsymbol{u} : \nabla \boldsymbol{v} \, \mathrm{d}\boldsymbol{x} + \int_{V_f} \rho[(\boldsymbol{u} \cdot \nabla)\boldsymbol{u}] \cdot \boldsymbol{v} \, \mathrm{d}\boldsymbol{x} = \int_{V_f} \boldsymbol{f} \cdot \boldsymbol{v} \, \mathrm{d}\boldsymbol{x}, \forall \boldsymbol{v} \in \tilde{V}_0, \\ \boldsymbol{u} = \boldsymbol{g} \text{ on } \Gamma. \end{aligned}\right\} \quad (A\,4)$$

This form lends itself to an equivalent minimization problem for $\boldsymbol{u}$

$$\left.\begin{aligned} J(\boldsymbol{u}) < J(\boldsymbol{w}), \ \forall \boldsymbol{w} \in \tilde{V}_g, \\ J(\boldsymbol{w}) = \tfrac{1}{2}\mu \int_{V_f} |\nabla \boldsymbol{\xi}(\boldsymbol{w})|^2 \, \mathrm{d}\boldsymbol{x}. \end{aligned}\right\} \quad (A\,5)$$

Problem (A 5) has the structure of a control problem where the state equation for $\boldsymbol{\xi}$ is governed by the Stokes equation for the velocity–pressure pair (ξ, π)

$$\left.\begin{aligned} \int_{V_f} (\nabla \cdot \boldsymbol{\xi})q \, \mathrm{d}\boldsymbol{x} = 0, \\ \int_{V_f} \mu \nabla \boldsymbol{\xi} : \nabla \boldsymbol{v} \, \mathrm{d}\boldsymbol{x} - \int_{V_f} \pi(\nabla \cdot \boldsymbol{v}) \, \mathrm{d}\boldsymbol{x} = \int_{V_f} \mu \nabla \boldsymbol{w} : \nabla \boldsymbol{v} \, \mathrm{d}\boldsymbol{x} + \int_{V_f} \rho[(\boldsymbol{w} \cdot \nabla)\boldsymbol{w}] \cdot \boldsymbol{v} \, \mathrm{d}\boldsymbol{x} - \int_{V_f} \boldsymbol{f} \cdot \boldsymbol{v} \, \mathrm{d}\boldsymbol{x}, \\ \boldsymbol{\xi} = 0 \text{ on } \Gamma. \end{aligned}\right\}$$

$$(A\,6)$$

Glowinski (1984) shows that the solution to the minimization problem (A 5) occurs when $\boldsymbol{\xi} = 0$ which then yields $J(\boldsymbol{u}) = 0$. The minimizing $\boldsymbol{u}$ is also the solution to (A 4), and because it is in the space $\tilde{V}_g$, $\boldsymbol{u}$ also solves (8). The pressure satisfying (8) is then given by $p = -\pi$.

In practice, we replace all the above continuous formulations with the MINI finite element discretization previously discussed. In order to find the discrete minimizer $\boldsymbol{u}_h$, we employ a conjugate gradient algorithm, which requires the gradient of the functional, J. We present without details the variational derivative (Glowinski 1984),

$$\langle J'(\boldsymbol{w}), \boldsymbol{v} \rangle = \int_{V_f} \mu \nabla \boldsymbol{\xi} : \nabla \boldsymbol{v} \, \mathrm{d}\boldsymbol{x} + \int_{V_f} \rho [(\boldsymbol{v} \cdot \nabla)\boldsymbol{w}] \cdot \boldsymbol{\xi} \, \mathrm{d}\boldsymbol{x} + \int_{V_f} \rho [(\boldsymbol{w} \cdot \nabla)\boldsymbol{v}] \cdot \boldsymbol{\xi} \, \mathrm{d}\boldsymbol{x}, \quad \text{(A 7)}$$

which leads to the following algorithm.

Algorithm 2. Nonlinear least-squares conjugate gradient method for the discretized Navier–Stokes equations (Glowinski 1984).
For $\boldsymbol{u}_h^0 \in \tilde{V}_{gh}$, compute $\boldsymbol{z}_h^0$ by first determining $\boldsymbol{\xi}_h^0$ from

$$\left.\begin{aligned}
&\int_{V_f} (\nabla \cdot \boldsymbol{\xi}_h^0) q_h \, \mathrm{d}\boldsymbol{x} = 0, \\
&\int_{V_f} \mu \nabla \boldsymbol{\xi}_h^0 : \nabla \boldsymbol{v}_h \, \mathrm{d}\boldsymbol{x} - \int_{V_f} \pi_h^0 (\nabla \cdot \boldsymbol{v}_h) \, \mathrm{d}\boldsymbol{x} = \int_{V_f} \mu \nabla \boldsymbol{u}_h^0 : \nabla \boldsymbol{v}_h \, \mathrm{d}\boldsymbol{x} + \int_{V_f} \rho \left[(\boldsymbol{u}_h^0 \cdot \nabla) \boldsymbol{u}_h^0 \right] \cdot \boldsymbol{v}_h \, \mathrm{d}\boldsymbol{x}, \\
&\hspace{6cm} - \int_{V_f} \boldsymbol{f} \cdot \boldsymbol{v}_h \, \mathrm{d}\boldsymbol{x} \\
&\hspace{3cm} \boldsymbol{\xi}_h^0 = 0 \text{ on } \Gamma,
\end{aligned}\right\} \quad \text{(A 8)}$$

and then the preconditioned descent direction from

$$\left.\begin{aligned}
&\int_{V_f} (\nabla \cdot \boldsymbol{z}_h^0) q_h \, \mathrm{d}\boldsymbol{x} = 0, \\
&\int_{V_f} \mu \nabla \boldsymbol{z}_h^0 : \nabla \boldsymbol{v}_h \, \mathrm{d}\boldsymbol{x} - \int_{V_f} \zeta_h^0 (\nabla \cdot \boldsymbol{v}_h) \, \mathrm{d}\boldsymbol{x} = \langle J_h'(\boldsymbol{u}_h^0), \boldsymbol{v} \rangle.
\end{aligned}\right\} \quad \text{(A 9)}$$

Then set $\boldsymbol{d}_h^0 = -\boldsymbol{z}_h^0$ and for $k = 0, 1, 2, \ldots,$
1. Find the descent parameter α^k such that

$$\alpha^k = \operatorname*{Arg\,min}_{\alpha \in \boldsymbol{R}} \ J_h(\boldsymbol{u}_h^k + \alpha \boldsymbol{d}_h^k). \quad \text{(A 10)}$$

2. $\boldsymbol{u}_h^{k+1} = \boldsymbol{u}_h^k + \alpha^k \boldsymbol{d}_h^k$.
3. Determine the new descent direction by solving

$$\left.\begin{aligned}
&\int_{V_f} (\nabla \cdot \boldsymbol{z}_h^{k+1}) q_h \, \mathrm{d}\boldsymbol{x} = 0, \\
&\int_{V_f} \mu \nabla \boldsymbol{z}_h^{k+1} : \nabla \boldsymbol{v}_h \, \mathrm{d}\boldsymbol{x} - \int_{V_f} \zeta_h^{k+1} (\nabla \cdot \boldsymbol{v}_h) \, \mathrm{d}\boldsymbol{x} = \langle J_h'(\boldsymbol{u}_h^{k+1}), \boldsymbol{v} \rangle.
\end{aligned}\right\} \quad \text{(A 11)}$$

4. Compute

$$\beta^{k+1} = \frac{\mu \displaystyle\int_{V_f} \nabla z_h^{k+1} : \nabla\left(z_h^{k+1} - z_h^k\right) \mathrm{d}x}{\mu \displaystyle\int_{V_f} \nabla z_h^k : \nabla z_h^k \, \mathrm{d}x}. \tag{A 12}$$

5. $d_h^{k+1} = -z_h^{k+1} + \beta^{k+1} d_h^k$.

In order to solve step 1 in this algorithm, we implement the strategy of Bristeau *et al.* (1985). Each iteration of algorithm 2 requires the solution of three discrete Stokes problems: one for the descent direction and then two to determine the descent parameter α. The conjugate gradient method described by Braess (1997) is used to solve each of these Stokes problems. We continue algorithm 2 until the discrete momentum residual, equation (9), has no component larger than 1×10^{-5}. This tolerance almost always coincides with $J_h(u_h^0)/J_h(u_h^{k+1}) < 10^6$.

REFERENCES

AIDUN, C. K., LU, Y. & DING, E.-J. 1998 Direct analysis of particulate suspensions with inertia using the discrete Boltzmann equation. *J. Fluid Mech.* **373**, 287–311.

ARNOLD, D., BREZZI, F. & FORTIN, M. 1984 A stable finite-element method for the Stokes equations. *Calcolo* **4**, 337.

BAGCHI, P. & BALACHANDAR, S. 2002 Steady planar straining flow past a rigid sphere at moderate Reynolds number. *J. Fluid Mech.* **466**, 365–407.

BAGCHI, P. & BALACHANDAR, S. 2003 Inertial and viscous forces on a rigid sphere in straining flows at moderate Reynolds numbers. *J. Fluid Mech.* **481**, 105–148.

BATCHELOR, G. K. 1970 The stress system in a suspension of force-free particles. *J. Fluid Mech.* **41**, 545–570.

BOTTIN, S., DAUCHOT, O. & DAVIAUD, F. 1997 Intermittency in a locally forced plane Couette flow. *Phys. Rev. Lett.* **79**, 4377–4380.

BOTTIN, S., DAUCHOT, O., DAVIAUD, F. & MANNEVILLE, P. 1998 Experimental evidence of streamwise vortices in transitional plane Couette flow. *Phys Fluids* **10**, 2597–2607.

BRADY, J. F. & MORRIS, J. F. 1997 Microstructure of a strongly sheared suspension and its impact on rheology and diffusion. *J. Fluid Mech.* **348**, 103–139.

BRAESS, D. 1997 *Finite Elements*. Cambridge University Press.

BRISTEAU, M. O., GLOWINSKI, R., MANTEL, B., PERIAUX, J. & PERRIER, P. 1985 Numerical methods for incompressible and compressible Navier–Stokes problems. *Finite Elements Fluids* **6**, 1.

DANDY, D. S. & DWYER, H. A. 1990 A sphere in shear flow at finite Reynolds number: effect of shear on particle lift, drag, and heat transfer. *J. Fluid Mech.* **216**, 381–410.

DING, E.-J. & AIDUN, C. K. 2000 The dynamics and scaling law for particles suspended in shear flow with inertia. *J. Fluid Mech.* **423**, 317–344.

FORNBERG, B. 1985 Steady viscous flow past a circular cylinder up to Reynolds number 600. *J. Comput. Phys.* **61**, 297.

FORNBERG, B. 1988 Steady viscous flow past a sphere at high Reynolds numbers. *J. Fluid. Mech.* **190**, 471–489.

GLOWINSKI, R. 1984 *Numerical Methods for Nonlinear Variational Problems*. Springer.

GRESHO, P. M. & SANI, R. L. 1998 *Incompressible Flow and the Finite-Element Method: Advection–Diffusion and Isothermal Laminar Flow*. Wiley.

HIGDON, J. J. L. 1993 The kinematics of the four-roll mill. *Phys. Fluids* A **5**, 274–276.

HOLST, M., BAKER, N. & WANG, F. 2000 Adaptive multilevel finite element solution of the Poisson–Boltzmann equation I: algorithm and examples. *J. Comput. Chem.* **21**, 1319.

HUANG, P. Y. & JOSEPH, D. D. 2000 Effects of shear thinning on migration of neutrally-buoyant particles in pressure driven flow of Newtonian and viscoelastic fluid. *J. Non-Newtonian Fluid Mech.* **90**, 159.

JEFFREY, D. J., MORRIS, J. F. & BRADY, J. F. 1993 The pressure moments for two spheres in a low-Reynolds-number flow. *Phys. Fluids* A **5**, 2317.

KIM, S. & KARRILA, S. 1991 *Microhydrodynamics: Principles and Selected Applications.* Butterworth-Heinemann.

KOCH, D. L. & HILL, R. J. 2001 Inertial effects in suspension and porous-media flows, *Annu. Rev. Fluid Mech.* **33**, 619–647.

KOSSACK, C. A. & ACRIVOS, A. 1974 Steady simple shear flow past a cirular cylinder at moderate Reynolds number: a numerical solution. *J. Fluid Mech.* **66**, 353–376.

LEGENDRE, D. & MAGNAUDET, J. 1998 The lift force on a spherical bubble in a viscous linear shear flow. *J. Fluid Mech.* **368**, 81–126.

LIN, C. J., PEERY, J. H. & SCHOWALTER, W. R. 1970 Simple shear flow round a rigid sphere: inertial effects and suspension rheology. *J. Fluid Mech.* **44**, 1–17.

MATAS, J.-P., MORRIS, J. F. & GUAZZELLI, É. 2003 Transition to turbulence in particulate pipe flow, *Phys. Rev. Lett.* **90**, 014501.

MOON, P. & SPENCER, D. E. 1971 *Field Theory Handbook.* Springer.

NIRSCHL, H., DWYER, H. A. & DENK, V. 1995 Three-dimensional calculations of the simple shear flow around a single particle between two moving walls. *J. Fluid Mech.* **283**, 273–285.

PATANKAR, N. A. & HU, H. H. 2002 Finite Reynolds number effect on the rheology of a dilute suspension of neutrally buoyant circular particles in a Newtonian fluid. *Intl J. Multiphase Flow* **28**, 409–425.

PHUNG, T. N., BRADY, J. F. & BOSSIS, G. 1996 Stokesian Dynamics simulation of Brownian suspensions. *J. Fluid Mech.* **313**, 181–207.

POE, G. G. & ACRIVOS, A. 1975 Closed streamline flows past rotating single spheres and cylinders: inertia effects. *J. Fluid Mech.* **72**, 605–623.

ROBERTSON, C. R. & ACRIVOS, A. 1970 Low Reynolds number shear flow past a rotating circular cylinder. Part 1. Momentum transfer. *J. Fluid Mech.* **40**, 685–704.

RUSSEL, W. B., SAVILLE, D. A. & SCHOWALTER, W. R. 1989 *Colloidal Dispersions.* Cambridge University. Press.

RYSKIN, G. 1980 The extensional viscosity of a dilute suspension of spherical particles at intermediate microscale Reynolds numbers. *J. Fluid Mech.* **99**, 513–529.

STONE, H. A., BRADY, J. F. & LOVALENTI, P. M. 2001 Inertial effects on the rheology of suspensions and on the motion of individual particles. Submitted to *J. Fluid Mech.*

SUNDARESAN, S., EATON, J. K., KOCH, D. L. & OTTINO, J. M. 2003 Appendix 2: Report of study group on disperse flow. *Intl J. Multiphase Flow* **29**, 1069–1087.

THOMMASET, F. 1981 *Implementation of Finite Element Methods for Navier–Stokes Equations.* Springer.

ZETTNER, C. M. & YODA, M. 2001a The circular cylinder in simple shear at moderate Reynolds number: An experimental study. *Exps. Fluids* **30**, 346–353.

ZETTNER, C. M. & YODA, M. 2001b Moderate-aspect-ratio elliptical cylinders in simple shear with inertia. *J. Fluid Mech.* **442**, 241–266.